JGR Oceans

RESEARCH ARTICLE
10.1029/2020JC016670

Special Section:
The Arctic: An AGU Joint Special Collection

Large Mesoscale Eddies in the Western Arctic Ocean From Satellite Altimetry Measurements

A. A. Kubryakov[1], I. E. Kozlov[1], and G. E. Manucharyan[2]

[1]Marine Hydrophysical Institute of RAS, Sevastopol, Russia, [2]School of Oceanography, University of Washington, Seattle, DC, USA

Key Points:

- Altimetry data reveals that large mesoscale eddies are abundant in the seasonally ice-free Western Arctic Ocean
- The eddy hot spots in the study region are the Amundsen Gulf, Mackenzie River mouth, the western Beaufort Sea, and the Chukchi Sea
- The interannual variability of eddy number and intensity is mainly driven by the intensity of the anticyclonic Beaufort Gyre

Correspondence to:
A. A. Kubryakov,
arskubr@gmail.com

Citation:
Kubryakov, A. A., Kozlov, I. E., & Manucharyan, G. E. (2021). Large mesoscale eddies in the Western Arctic Ocean from satellite altimetry measurements. *Journal of Geophysical Research: Oceans*, *126*, e2020JC016670. https://doi.org/10.1029/2020JC016670

Received 5 AUG 2020
Accepted 5 APR 2021

Abstract Eddies in the Western Arctic play an important role in transporting heat, salt, and biogeochemical tracers across the continental shelf and within the deep basins. However, comprehensive observations of the regional and temporal variability of the eddy field characteristics are difficult to obtain remotely due to the presence of sea ice, and the available in situ observations remain relatively sparse. Nonetheless, with continuing global warming, increasingly large areas of the Arctic Ocean become seasonally ice-free and can be observed with remote sensing. Here, we use satellite altimetry data acquired between 1993 and 2018 over the seasonally ice-free Western Arctic Ocean to detect the signatures and hot spots of large mesoscale eddies, validating their detection method using independent optical and infrared satellite observations. The altimetry measurements were most frequent from July to October, revealing signatures of over 2000 individual eddies that were roughly equally partitioned between cyclones and anticyclones, with radii between 20 and 60 km and characteristic orbital velocities of about 0.05–0.4 m/s. A maximum number of eddies were detected in October in the Beaufort Sea and in November in the Chukchi Sea. The interannual variability of eddies in the Beaufort Sea is correlated with variations of intensity and freshwater content in the Beaufort Gyre. Using the regional eddy statistics, we discuss the potential eddy formation mechanisms over the key regions of their observations in the Amundsen Gulf, the area adjacent to the Mackenzie River mouth, the western part of the Beaufort Sea, and the Chukchi Sea.

Plain Language Summary Ocean dynamics at scales greater than about 10 km are dominated by energetic eddies but are hard to observe in the Arctic Ocean because of sea ice. Eddies affect the horizontal exchange of heat, salt, and nutrients, changing the thermohaline structure and ecosystem of the Arctic Ocean. Here, we present the first comprehensive study of eddy statistics in ice-free regions of the western Arctic Ocean using frequent satellite observations of sea surface height from 1993 to 2018. Using an automated detection method that we validated with satellite optical images, we quantify the eddies' pathways, shape, and dynamics, and their spatial and interannual variability. Due to the comprehensive spatial coverage of altimetry satellites, we were able to identify hot spots of eddy generation in the study region: the entrance to the Amundsen Gulf, the area near the Mackenzie River mouth, the western part of the Beaufort Sea, and the Chukchi Sea.

1. Introduction

Eddies in the Western Arctic play an important role in transporting heat and salt from the continental shelf to the deep basin (e.g., D'Asaro, 1988; Manley & Hunkins, 1985). They are also linked to the redistribution of freshwater within the surface-stress-driven Beaufort Gyre (BG) and the BG's stabilization, contributing significantly to overall along-isopycnal mixing in the Arctic Ocean (Doddridge et al., 2019; Manucharyan et al., 2017; Manucharyan & Spall, 2015; Meneghello et al., 2017, 2020; Spall et al., 2008; Timmermans & Marshall, 2020). Eddies can noticeably impact the thermohaline structure of the basin and its stratification, thereby strongly modifying vertical mixing patterns (Watanabe et al., 2014). In the western Arctic, eddies contribute to the transfer of warm, fresh, and nutrient-rich Pacific-origin water into the Canada Basin. They provide a cross-isobath nutrient flux from the highly productive zones adjacent to the mouth of the Mackenzie River, fueling the marine ecosystem in the central parts of the Arctic Ocean (Watanabe et al., 2012, 2014).

The properties and dynamics of eddies have been extensively studied in several parts of the study region using CTD and current meter data (D'Asaro, 1988; Manley & Hunkins, 1985; Mathis et al., 2007; Muench et al., 2000; Newton et al., 1974; Scott et al., 2019), Ice-Tethered Profilers (ITPs) (Timmermans et al., 2008; Zhao et al., 2016), drifters (Mensa et al., 2018), microstructure measurements (Fine et al., 2018; Padman et al., 1990), satellite observations (Kozlov et al., 2019; Watanabe et al., 2012), and modeling (Brannigan et al., 2017; Meneghello et al., 2021; Spall, 2008; Watanabe, 2011). Observations using ITP profilers (Timmermans et al., 2007; Zhao et al., 2014, 2016) were used to obtain statistical eddy properties in the deep and shelf areas of the Beaufort Sea (BS) and study the impact of eddies on the thermohaline structure of the basin. In situ investigations show that the most frequently detected eddies had relatively small radii (5–10 km), in agreement with the small values of the first and the second mode Rossby deformation radii, R_i, in the Arctic Ocean (Nurser & Bacon, 2014), and orbital velocities in the range of 0.1–0.4 m/s. These studies also showed that anticyclonic eddies were significantly more abundant than cyclonic eddies(Manley & Hunkins, 1985; Newton et al., 1974; Timmermans et al., 2008; Zhao et al., 2014, 2016).

Many in situ studies have been directed to the investigation of the shelf break eddies of the Alaskan Coastal Current. They demonstrate several important mechanisms of eddy generation, such as baroclinic instability and buoyant forcing caused by inflowing Pacific Ocean waters (Pickart et al., 2005; Spall et al., 2008; Watanabe, 2011), and current-topography interactions such as topographic drag in the Barrow Canyon (D'Asaro, 1988). In the deep Canada Basin, the formation of eddies is attributed to the baroclinic instability of the boundary currents (Manley & Hunkins, 1985) and frontal dynamics (Manucharyan & Timmermans, 2014; Spall, 1995; Timmermans et al., 2008).

Kozlov et al. (2019) provide detailed information on spatial distribution, size, and vorticity sign of eddies in the western Arctic based on high-resolution spaceborne synthetic aperture radar (SAR) data. SAR observations effectively trace eddy signatures in the surface roughness fields due to wave-current interactions and spatial redistribution of surfactant films and sea ice by eddy-induced surface currents. In particular, the authors emphasize the clear dominance of small cyclonic eddies at the surface of the ocean, contrary to in-situ observations of halocline eddies dominated by anticyclonic eddies (Zhao et al., 2014). In addition, the surface anticyclonic eddies statistically had larger scales than cyclonic eddies, reaching diameters up to 50–100 km (Kozlov et al., 2019) that are substantially larger than the O(10 km) in situ halocline eddies (Timmermans et al., 2008; Zhao et al., 2014). While these SAR observations have provided a detailed record of spatial eddy properties over the ice-free ocean and in the marginal ice regions, they were inevitably lacking the information about such dynamically relevant eddy characteristics as orbital velocity, vorticity, translational speed, and lifetime. Instead, such information can be obtained from satellite altimetry data, which provides continuous measurements of the dynamic characteristics of the ocean at scales of 10–100 km.

Satellite altimetry can be used to effectively track the evolution of the dynamic characteristics of individual eddies. Methods of automated eddy identification from altimetry data give a vast amount of statistical information on the spatial and temporal variability of different eddy properties (size, orbital velocity, polarity, lifetime, and others), their trajectories, and dynamic structure on global scales (Chelton et al., 2011), as well as over the specific regions of the World Ocean (e.g., Chaigneau et al., 2011; Chen et al., 2011; Kubryakov & Stanichny, 2015b Kubryakov et al., 2016). Such methods have previously been applied in the high latitudes to successfully study characteristics of the large eddies in the Norwegian Sea (Bashmachnikov et al., 2018; Raj et al., 2016), and the North Greenland Sea and Fram Strait (Bashmachnikov et al., 2020).

In the Arctic Ocean, the use of altimetry data has several restrictions. Many satellites (TOPEX/Poseidon and Jason series) have a maximum latitude of 66° and, hence, do not obtain measurements over this region. Moreover, the Arctic basin is characterized by small values of the Rossby radius, R_i, typically ~5–15 km (Nurser & Bacon, 2014). Small eddies of the order of R_i cannot be effectively detected in current altimetric data. Nonetheless, studies of high-latitude eddies demonstrate that characteristic eddy sizes often significantly exceed the R_i (Sévigny et al., 2015; Watanabe, 2011; Wood et al., 2015). For example, Watanabe (2011) used satellite infrared data to demonstrate the presence of large eddies around 70 km in diameter near the Beaufort shelf break. Sévigny et al. (2015) also documented an eddy in the northern part of the Amundsen Gulf with a diameter of 40 km, where R_i is less than 10 km. The presence of eddies with radii much larger than R_i is consistent with the inverse energy cascade when the beta-effect is weak (Larichev & Held, 1995), as in high-latitude oceans. For example, idealized numerical experiments of the Ekman-driven

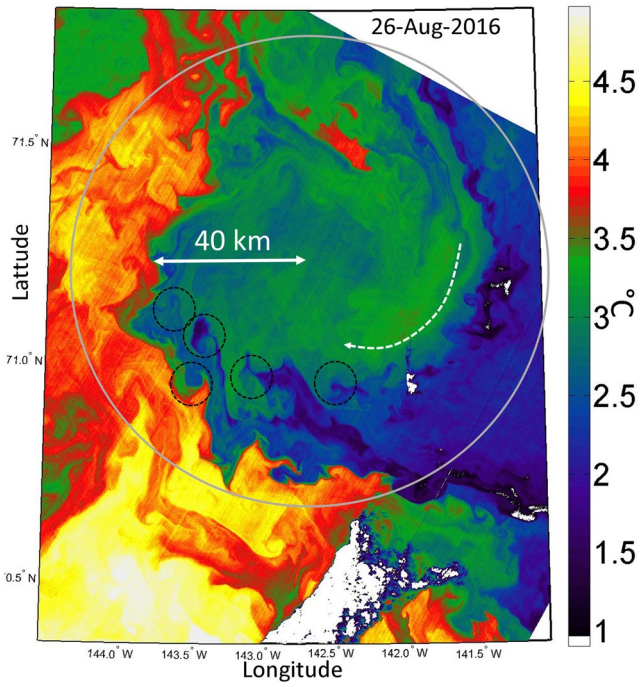

Figure 1. Large mesoscale anticyclone observed in Landsat-8 thermal image (brightness temperature in channel 11, °C) on August 26, 2016 (gray circle) on the Beaufort Sea shelf. White color marks clouds. Black circles show the submesoscale cyclonic eddies formed on the periphery of the large anticyclone. The white dashed arrow shows the direction of eddy rotation.

BG (Manucharyan et al., 2017; Manucharyan & Spall, 2015; Meneghello et al., 2018) generate eddies that are O(100 km) in size. Note that eddies of various horizontal scales would also vary in their vertical extent and baroclinic mode structure. In this manuscript, we bring attention to the relatively large-scale eddies with detectable surface expressions.

As an example, Figure 1 demonstrates the manifestation of such a large anticyclonic eddy on the Landsat-8 thermal image acquired over the central part of the BS shelf on August 26, 2016. The radius of the eddy is about 40 km, which is about three times larger than the climatological value of R_i(13 km) in this region (Nurser & Bacon, 2014). This anticyclone traps the warm shelf waters from the southwest and transports them to the northeast. A fraction of these warm waters is also accumulated in the eddy center due to the convergence induced by downwelling in the anticyclone (McGillicuddy & Robinson, 1997). At the same time, the eddy entrains cold Arctic waters on its eastern periphery and transports them to the west. Strain and horizontal shear of orbital velocity on the periphery of anticyclones (see e.g., Brannigan et al., 2017; Elkin & Zatsepin, 2014; Kozlov et al., 2020; Manucharyan & Timmermans, 2014; Zatsepin et al., 2019;) cause the formation of the number of small submesoscale cyclones with radii of 1–5 km on its southern periphery (black circles in Figure 1b). Such submesoscale eddies may induce intense vertical velocities reaching up to 10–100 m/day (see e.g., McWilliams et al., 2016), and thus can strongly impact the nutrient fluxes (Watanabe et al., 2014) and the stratification in the basin. Thereby, large eddies similar to the one presented in Figure 1a may have a strong impact on the thermohaline structure, dynamics, and ecosystem of the Arctic Ocean.

In this study, we use satellite altimetry data to identify relatively large mesoscale eddies with radii more than 20 km, that is, two or more times larger than R_i, over the seasonally ice-free Western Arctic Ocean during the 1993–2018 period. The obtained results are validated using satellite optical and infrared data. We investigate the general characteristics of these eddies, including their spatial distribution, size, trajectories, and orbital velocities. Furthermore, we identify and then focus on several regions of high eddy activity-entrance to the Amundsen Gulf, the area adjacent to the Mackenzie River mouth, the western part of the BS, and the Chukchi Sea (CS)—to analyze seasonal and interannual variability of eddy properties during an ice-free season and possible mechanisms responsible for their formation.

2. Data and Methods

2.1. Altimetry Data

In this study, we investigate the eddy properties over the large domain within latitudes of 65–78°N and longitudes from −180°W to −115°W, covering the CS, the Beaufort Sea and the Amundsen Gulf from daily gridded satellite altimetry data (see Figures 2a and 2c). We obtained the gridded altimetry data (product identifier: SEALEVEL_GLO_PHY_L4_REP_OBSERVATIONS_088_047) for 1993–2018 from the Copernicus Marine Environmental Monitoring Service (CMEMS). This product consists of daily gridded maps of dynamic topography in ice-free regions that have been derived as a sum of mapped sea level anomalies (SLAs) calculated from combined measurements by different satellites (https://duacs.cls.fr) and mean dynamic topography (MDT) from Rio et al. (2013). The data are corrected for instrumental errors, tidal influence, wind, and pressure effects, and objectively interpolated to a 1/4° Mercator projection grid (Le Traon et al., 1998). Note, however, that this grid (roughly 28 × 7 km at 75°N) does not resolve the ocean variability at the small scales of R_i for high latitudes.

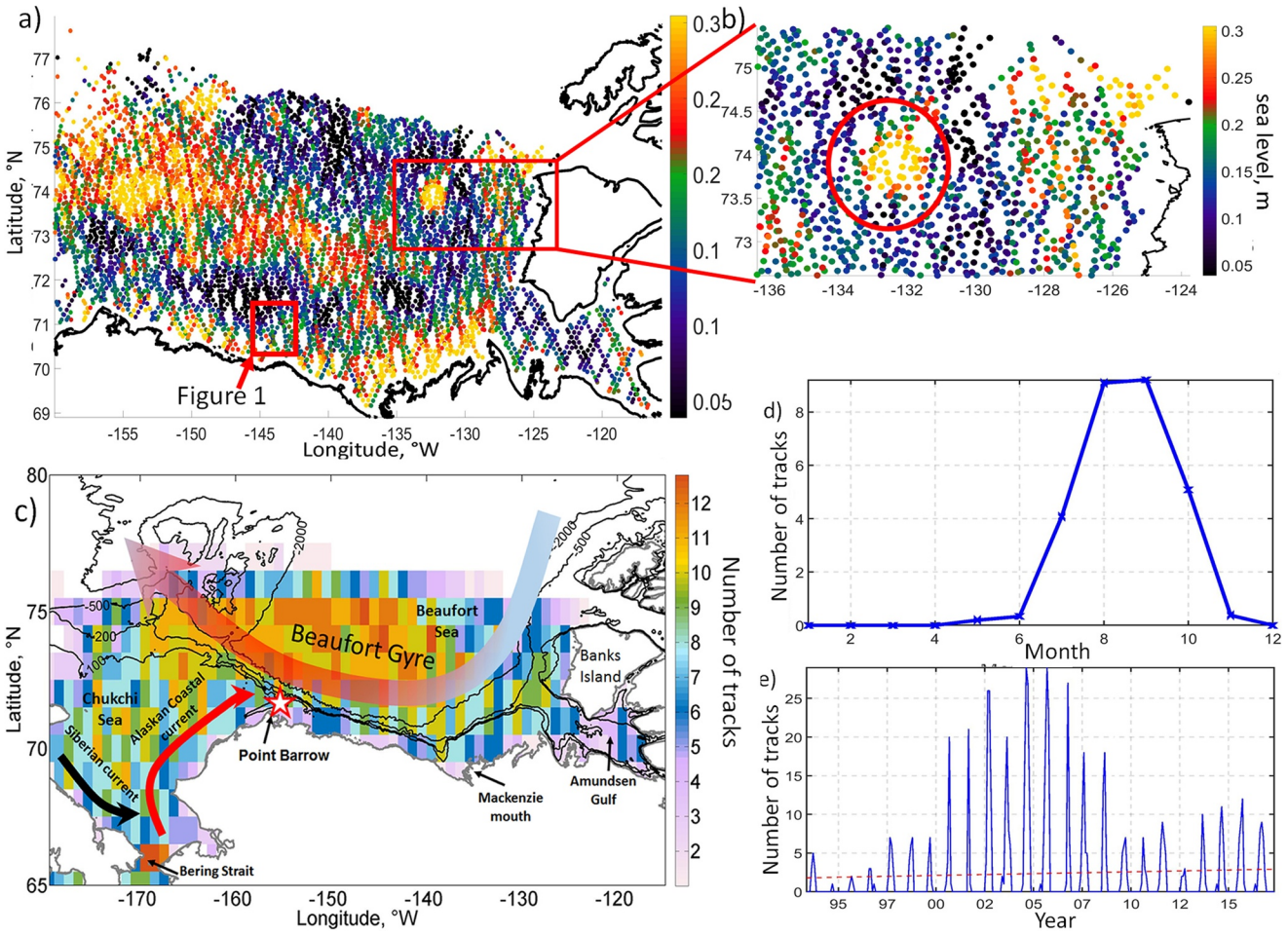

Figure 2. (a) Sea level distribution (m) from the along-track altimetry measurements in September 2016. Red rectangle shows the position of the eddy shown in Figure 1a; (b) zoomed part of the map shown in (a), red circle shows the position of an anticyclone with a radius of 40 km; (c) the number of altimetry tracks crossing 1 × 1° bin in September 2016; (d) seasonal variability of the mean number of altimetry tracks during 1993–2016 available per month in 1 × 1° bin near Point Barrow (72°N, −157°W) shown as a white star in (c); (e) interannual variability of the mean number of altimetry tracks available per month near Point Barrow.

Geostrophic velocities are then computed from the gradients of sea level as $u_g = \frac{g}{f}\frac{\partial h}{\partial y}$; $v_g = \frac{g}{f}\frac{\partial h}{\partial x}$ where u_g and v_g are the zonal and meridional components of geostrophic velocity, h is the dynamic topography, f is the Coriolis parameter, and g is the gravitational acceleration. The data on geostrophic velocity are distributed by CMEMS in the same product.

Only altimetry satellites with high-inclination orbits provide useful information in high-latitude regions; this excludes the TOPEX/Poseidon and Jason series of satellites. However, several altimetry missions do cover our study; these are ERS-1 (1991–1996), ERS-2 (1996–2003), Envisat (2002–2012), GEOSAT Follow-On (GFO) (1998–2006), Cryosat-2 (2010–present), SARAL (2013–present), and Sentinel-3 A/B (2016–present). Note, however, that altimetric sea level data is not presently available over ice-covered areas.

At the same time, the convergence of satellite tracks increases the spatio-temporal resolution of altimetry data at high latitudes. Quantitative validation of altimetry data on sea level in the Arctic basin has been documented in several studies (see e.g., Naumov et al., 2019; Volkov & Pujol, 2012). Volkov and Pujol (2012) showed that altimetry data generally match tide gauge data and the standard deviation between them, partly related to the differences in the measurements position, varies from 2 to 12 cm. That study also compared drifter and altimetry-derived data on current velocity and showed that mapped altimetry data was able to

reproduce mesoscale variability of the velocity. The possibility of resolving mesoscale eddy properties was later confirmed for the Barents Sea (Volkov et al., 2013), the Norwegian Sea (Bashmachnikov et al., 2018; Raj et al., 2016), the North Greenland Sea, and Fram Strait (Bashmachnikov et al., 2020) on the base of various eddy identification methods.

To estimate the number of available altimetry tracks over the study region we use along-track sea SLA data downloaded from CMEMS (product SEALEVEL_GLO_PHY_L3_REP_OBSERVATIONS_008_062). Figure 2a shows an example of along-track SLA data over the study region in September 2016. The study region including the CS and the BS is covered by a dense number of satellite tracks with relatively small gaps between the adjacent tracks, often less than 10 km. The zoomed image in Figure 2b demonstrates the clear manifestation of a large anticyclonic eddy, seen as a round area with increased sea level. The radius of such eddy centered at 74°N latitude is about 40 km, similar to the eddy shown in Figure 1 that was observed in thermal imagery. Its orbital velocity, estimated from the along-track altimetry data, reaches about 0.4–0.5 m/s.

Altimetry maps are produced using spatial interpolation of the along-track data with a window size of about 1° (Pascual et al., 2006). To estimate the amount of the along-track data used for the reconstruction of the gridded sea level maps we calculate the number of available altimetry tracks over the ice-free regions crossing the 1 × 1° bin. The example for September 2016 is shown in Figure 2c. On average, each 1 × 1° bin is covered by 8–12 altimeter tracks. This is even more frequent than is usually available in mid- and low latitudes. For example, at 45°N, only about six to eight different tracks cross a 1 × 1° bin per month.

The number of available altimetry data at a given location varies significantly depending on two main factors: the presence of sea ice cover and the number and the orbit characteristics of working altimetric satellites. As an example, Figure 2d shows seasonal variability of the number of tracks available per month over the 1 × 1° bin located north of Point Barrow (72°N, 157°E) marked as a red star in Figure 2c. The ice cover is smallest in June–October with a minimum in September, which defines the seasonal peak of available altimetry tracks in Figure 2d, on average reaching eight to nine tracks per month in 1993–2016. There are almost no available measurements during the cold season from January to April, very few in May–June and November–December (less than one per month). In November–December, standard altimetry data are available only over the CS, which is partly ice-free due to the inflow of warm Pacific-origin water (Figure 2d). To account for this effect, the statistics of eddy numbers presented below are normalized on the number of available ice-free altimetry data. For this task, we use the parameter hereinafter called the probability of eddy observations, P, defined as the number of days during which an eddy is observed divided by the number of days with available altimetry data over that same grid box. For the temporal analysis, we compute a percentage of the area covered by eddies on a particular day relative to the total area with available altimetry data for that day, hereinafter, eddy-covered area S.

The number of measurements also significantly varies on interannual time scales (Figure 2e). The maximum number of tracks is available in 2001–2008 when this area was covered simultaneously by three satellites with high orbit inclination (GFO, ERS-2, Envisat). In this period, up to 15–20 altimetric tracks were available in a month in August–September in a 1 × 1° box, that is, the measurements were available almost every two days. During 1991–1996 and in 2012 only one such satellite was at work, resulting in only two tracks per month, while six tracks per month were available in 1998–2000 and 2009–2011. Such changes in the number of tracks can also affect the estimates of time variability of eddy properties derived from satellite altimetry data.

2.2. Eddy Identification

Mesoscale eddy dynamics are investigated using a "winding angle" automated eddy identification method, which is based on the detection of closed streamlines in the geostrophic velocity field (Sadarjoen & Post, 2000). This method is widely used for eddy identification in the ocean (e.g., Chaigneau et al., 2008; Chen et al., 2011; Kubryakov & Stanichny, 2015a, 2015b; Souza et al., 2011). To identify the closed streamlines, Lagrangian particles are released in each grid point of the steady velocity field. For each particle, the trajectory and the total angle of deflection (winding angle) are calculated on each time step during the integration time. If the winding angle exceeds 360°, the starting grid point is situated on the closed streamline

and is marked as an "eddy point." Furthermore, data on the vorticity of the cluster of points is used to distinguish cyclonic and anticyclonic eddies, hereinafter, CEs and AEs, respectively. The following parameters are used in the method: maximum radius of an eddy should not exceed 70 km; the maximal period of rotation of a particle in the eddy should be higher than 70 days, which limits minimal available orbital velocity in the eddies. These criteria allow avoiding the identification of the weak large-scale gyres or very weak small eddies. The details of the algorithm are given in Kubryakov and Stanichny (2015a).

Due to the low resolution of the altimetry data, only eddies with radii above 24 km can be detected (i.e., eddies that occupy at least eight bins in a 0.25° grid, which corresponds to 25 × 10 km at 70°N). This lower limit is in good agreement with the estimates of the effective resolution of altimetry data given by Chelton et al. (2011) and Ballarotta et al. (2019). These authors show that eddies with a radius of 0.4° (corresponding to 28 × 7 km at 70°N) (Chelton et al., 2011) and 25 km (Ballarotta et al., 2019) can be effectively identified in altimetry data. Note that, at this spatial scale, the altimetry-derived dynamic topography will be smoothed due to spatio-temporal interpolation performed during the mapping procedure. This smoothing can result in the underestimation of eddy velocities by about a factor of two for the smallest eddies (Ballarotta et al., 2019; Chelton et al., 2011).

Our eddy tracking procedure is based on the detection of neighboring eddies of the same sign on two consecutive SLA maps. To avoid mischaracterizing two distinct eddies as a single eddy that has moved in space, the algorithm bounds the maximum distance the eddy can move per one day to 15 km. This criterion is based on the series of sensitivity tests and means that the maximum translational velocity of an eddy should not exceed 0.17 m/s. This assumption seems to be reasonable for the mesoscale eddies at high latitudes, at which the baroclinic speed of Rossby waves is small, and background currents are not intense (e.g., Armitage et al., 2016).

Note that eddies propagating under sea ice cannot be traced in the altimetry data; therefore, if at least a part of the eddy is located near the ice edge or within the ice-covered region, it is considered lost in the identification procedure. Consequently, the eddy lifetime based on open-ocean altimetry measurements can be underestimated because some eddies can move from or to the ice-covered regions. Thus, we define the quantity T as a "period of eddy observation" instead of "eddy lifetime." This value gives a lower estimate of the eddy lifetime, which defines the number of consecutive daily sea level maps in which we can detect the same eddy. For each eddy, we also define its radius (R), maximum orbital velocity (V_{max}), translational velocity (V_c), and eddy vorticity (Ω).

In this study, we use the daily gridded dataset of geostrophic velocity to identify the eddies. However, due to the spatio-temporal interpolation of the altimetry data eddies can sometimes be lost in consecutive daily fields of SLA. In this case, their trajectories will be interrupted. That is why T and eddy travel distance can be underestimated when using daily gridded altimetry data (Faghmous et al., 2015). To account for this effect, we also perform an eddy identification procedure on the base of 7-day averaged maps of SLA. The main results concerning spatial and temporal variability of the eddy properties are similar to those obtained on the base of daily maps. We also use the calculation based on 7-day averaged maps to estimate statistics on T in Figures 4a and 7c.

2.3. MODIS Visible and Infrared Data

Validation of the eddy identification and tracking algorithms was performed using imagery from the Moderate Resolution Imaging Spectroradiometer (MODIS). For this task, we use MODIS Level 3 daily and 8-day maps of chlorophyll *a* (chl-a) and sea surface temperature (SST) with a spatial resolution of 4 km (and 1 km for the inset shown in Figure 3a). Data for the 2003–2016 period was downloaded from the OceanColor data archive (http://oceancolor.gsfc.nasa.gov/). The data are routinely corrected for atmospheric and sea surface effects using standard atmospheric correction algorithms.

An example of eddies identified in altimetry data overlaid on an 8-day MODIS Aqua chl-a map centered on June 30, 2008 showing highly turbid Mackenzie River plume waters (Figure 3a) shows strong gradients that identify several mesoscale eddies on the periphery of the plume. A large cyclone (C1) is seen with a center at 71.3°N, 136.5°W. Its radius estimated from MODIS data is about 45 km. Another relatively large anticyclone (A1) with a 35 km radius is located to the west of it. Their sizes estimated from the altimetry data are

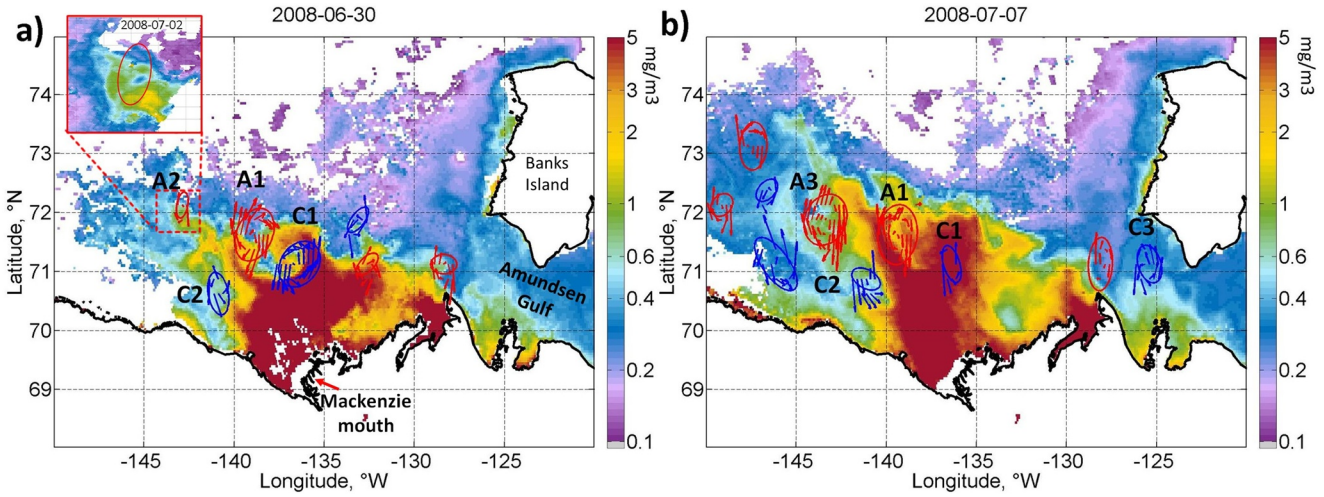

Figure 3. Eight-day MODIS Aqua chlorophyll *a* (chl-a) concentration maps (mg/m^3) centered at (a) June 30, 2008 and (b) July 7, 2008 with superimposed eddies identified in altimetry data (blue arrows—cyclones; red arrows—anticyclones). A red frame in the upper left corner of panel (a) shows a zoomed area of 1 km MODIS chl-a map depicting the small cyclone A2 (red ellipse).

similar to those obtained from the MODIS data. These eddies transport the water masses that are rich in chl-a northward, by the distances comparable to their diameters (50–100 km). Eddy-induced horizontal advection intensifies the spreading of the nutrient-rich waters to the deeper Canada Basin and thus can significantly affect the ecosystem of the central Arctic (Watanabe, Onodera, et al., 2014). Another cyclonic eddy (C2) with a radius of about 25 km is observed on the western periphery of the plume. A small anticyclonic eddy (A2) has also developed at the tip of a long filament spreading out from the northwest periphery of the plume. Its zoomed image obtained from 1 km resolution MODIS data is shown in the upper left corner of Figure 3a. Despite its small size, it can still be effectively identified by altimeters. Three more eddies are also identified by altimeters on the eastward periphery of the plume.

The next 8-day MODIS scene, centered on July 7, 2008 (Figure 3b), shows the evolution of the plume and the eddies. The large eddies observed at the offshore periphery of the plume have moved further northwest along with the plume front. More eddies are now identified by altimeters in the area west of the plume that became ice-free during the previous week. These "new" eddies are, however, poorly resolved in the 4-km MODIS product due to the absence or low concentration of tracers. Some eddies on the east side of the plume have disappeared. The anticyclone A1 and cyclones C1, C2 are still observed during the second week, and another large anticyclone A3 is identified on the western periphery of the plume. A cyclonic eddy C3 has appeared at the entrance of the Amundsen Gulf and will be discussed in detail in Section 4.1. Several other examples of algorithm validation with satellite imagery are given in Section 4.

2.4. Other Data

We use output from the MERRA-2 reanalysis (Gelaro et al., 2017) for 1993–2018 for the analysis of the wind velocity at 10 m height and sea ice concentration. The data are available from https://disc.gsfc.nasa.gov/datasets?project=MERRA-2. MERRA-2 is a modern NASA reanalysis that assimilates satellite data including data on sea ice concentration from passive microwave measurements.

Monthly discharge data of Mackenzie River for 1993–2016 was obtained from the Reference Hydrometric Basin Network, Canada (Brimley et al., 1999) at station Mackenzie River at Arctic Red River (67°27′21.6, 133°45′11.8), and downloaded from HYDAT database (https://collaboration.cmc.ec.gc.ca/cmc/hydrometrics/www/).

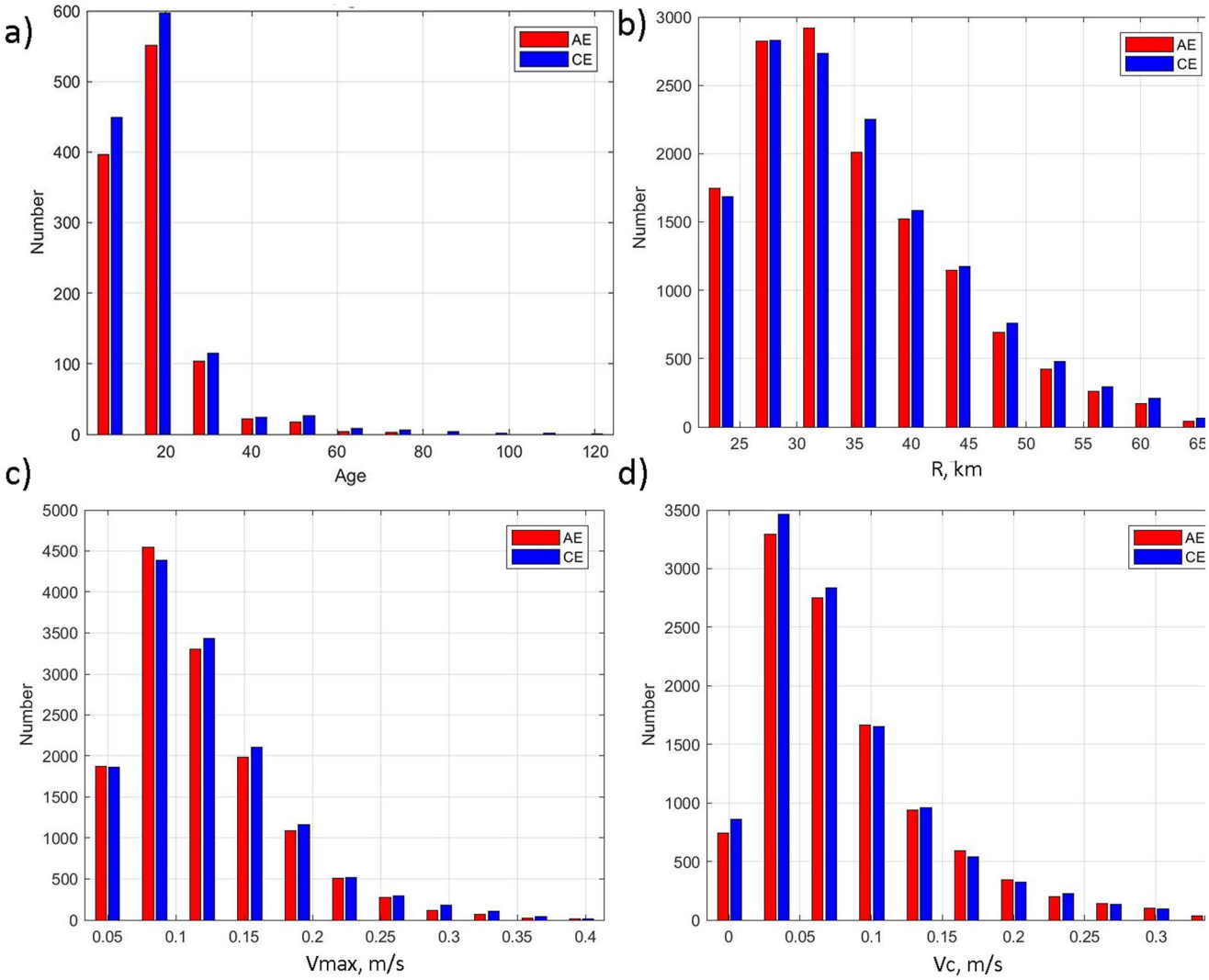

Figure 4. Statistical distributions of eddy parameters derived from satellite altimetry data: (a) period of eddy observation (T), day; (b) radius (R), km; (c) maximum orbital velocities (V_{max}), m/s; (d) translational velocity (V_c) of identified eddies, m/s. Statistics about the period of eddy observation were obtained using 7-day averaged altimetry maps: statistics of other properties were obtained using daily altimetry maps.

3. Eddy Characteristics

Analysis of daily gridded satellite altimetry products for 1993–2018 (9490 daily maps) over the entire study domain shown in Figure 2c (from 65° to 78°N and from −180° to −115°W) allow us to obtain 14,723 (15,008) identifications of CEs (AEs), which corresponds to 1179 (1186) individual CEs (AEs).

Eddy identification based on daily altimetry maps reveals 47 eddies with the period of eddy observation $T > 20$ days, 23 eddies with $T > 25$ days, and only six eddies with $T > 30$ days (not shown). We note that daily maps can contain uncertainties related to the daily temporal interpolation. We repeat the same eddy identification process with 7-day averaged maps. Such an analysis reveals many more long-lived eddies (Figure 4a). It identifies 75 eddies with $T > 1$ month, 12 eddies with $T > 2$ months, that is, they were tracked in more than four or eight consecutive 7-day maps. The trajectories of such eddies are shown in Figure S1d. Two cyclones situated to the northwest of the McKenzie River mouth at ~140°W and 71°N were traced for more than 3 months.

The distribution of observed eddy radii (R) peaks at about 30 km, reaching 60–65 km in some rare cases (Figure 4b). For eddy radii below 35 km, AEs were observed slightly more frequently than CEs, while CEs

dominate over AEs for radii above 35 km. Estimates of maximal eddy orbital velocity (V_{max}) peak near 0.1 m/s with maximal values up to 0.4 m/s (Figure 4c). The translational velocity (V_c) was generally between 0.01 and 0.06 m/s with a statistical peak at 0.035 m/s (Figure 4d).

The locations of the first encounter of eddies with $T > 2$ weeks are shown in Figure 5a. In the BS, most eddies were formed along the western periphery of the BG on the Chukchi/Beaufort shelf-slope boundary, over the continental slope in the south, near the Mackenzie River mouth, and in the Amundsen Gulf. A large number of eddies was also detected all over the CS inner and outer shelves. In CS, the highest number of eddies are detected in its southwestern coastal part and to the north of the Herald Shoal. Many eddies were also detected over the Chukchi Plateau extending up to 78°N. Satellite altimetry can detect eddies only over ice-free regions of the basin. That is why the obtained spatial distribution of eddies strongly correlates with the map of the average number of ice-free days per year shown in Figure 5a. This map was computed based on MERRA-2 reanalysis as an average number of days with ice concentration $C_{ice} < 15\%$. In the central and northern parts of the BG, where the ice cover persists throughout the year, eddies cannot be identified at all, but they are known to be present under the ice (e.g., Manley & Hunkins, 1985; Timmermans et al., 2008). The obtained altimetry-based eddy map shown in Figure 5b is also in good agreement with the results of spaceborne SAR observations (Kozlov et al., 2019) that provides detailed statistics of the small-scale eddies with diameters of 1–10 km (compare with Figure 5a in Kozlov et al., 2019). Due to land/ice contamination of the signal reflectance near the coast, velocity streamlines in the coastal eddies could not be closed. Therefore, our used algorithm cannot identify eddies near the coast.

The trajectories of eddies with $T > 2$ weeks (Figure 5c) demonstrate that most eddies propagate northward toward the deep basin over the continental slope in the southern BS. In the western and northwestern BS, eddies predominantly move to the northwest, while in its eastern part they move westward. This coincides well with the direction of the background anticyclonic current of the BG (see time-averaged geostrophic currents in Figure 6a) that seems to play an important role in the eddy translation. Northward trajectories are predominant over the northern and southern CS shelves. This direction is in agreement with the direction of the penetrating Pacific waters and the Alaskan Coastal Current.

The time-averaged map of eddy translational velocity indicates that V_c is directed poleward in most regions (Figure 6b), except in the eastern BS where it is directed southwest aligned with the BG. Translational velocities are highest in the northwestern part of the BS and in the western and eastern parts of the CS, where they on average reach 0.08–0.1 m/s. Three longitudinal bands (1, 2, and 3) of intense poleward eddy propagation are found at 175°W, 167°W, and 152°W. At these longitudes, the average background velocities are also directed to the north (Figure 6a), indicating the impact of the mean flow on the eddy movement. In particular, strong northward velocities of eddy translation are observed in the area of the Alaskan Coastal Current and the Chukchi/Beaufort shelf-slope boundary. The region centered at 152°W extends northward from 73°N to about 77°N in the deep Canada Basin, corresponding to the weaker northward branch of the BG located to the east of the main branch. The geostrophic currents in this branch are directed purely northward in agreement with the eddy propagation directions (Figure 6b). High values of poleward eddy translational velocity (0.05–0.07 m/s) are also observed near Mackenzie River mouth (arrow 4 in Figure 6b), where the generation of eddies is related to baroclinic instabilities on the edge of the Mackenzie River plume (see Section 4.2 for more details).

The probability of eddy observations, P, defined in Section 2.1 is shown in Figure 7a.

Four regions with increased eddy probability ($P > 0.1$) can be visually distinguished in this map (marked by red dashed boxes in Figure 7a). The first distinct zone is located at the entrance to the Amundsen Gulf (box 1 in Figure 7a). The second area is located to the west and northwest of the Mackenzie River mouth (box 2) and can be associated with the plume front, which is displaced westward by the action of the buoyant forcing and background geostrophic currents. The third area elongated from southwest to northeast is situated in the western part of the BS on the Chukchi/Beaufort shelf-slope boundary (box 3). It is related to the most intense part of the BG located in the region of interaction of the Pacific-origin and the Arctic waters (Figure 6a). The eddy activity is also intense in the CS (box 4), with maximal P found in its southern part near the Bering Strait, off its western coast, and to the north of Herald Shoal. The regional features of eddy dynamics in these four regions are discussed in more detail in Section 4.

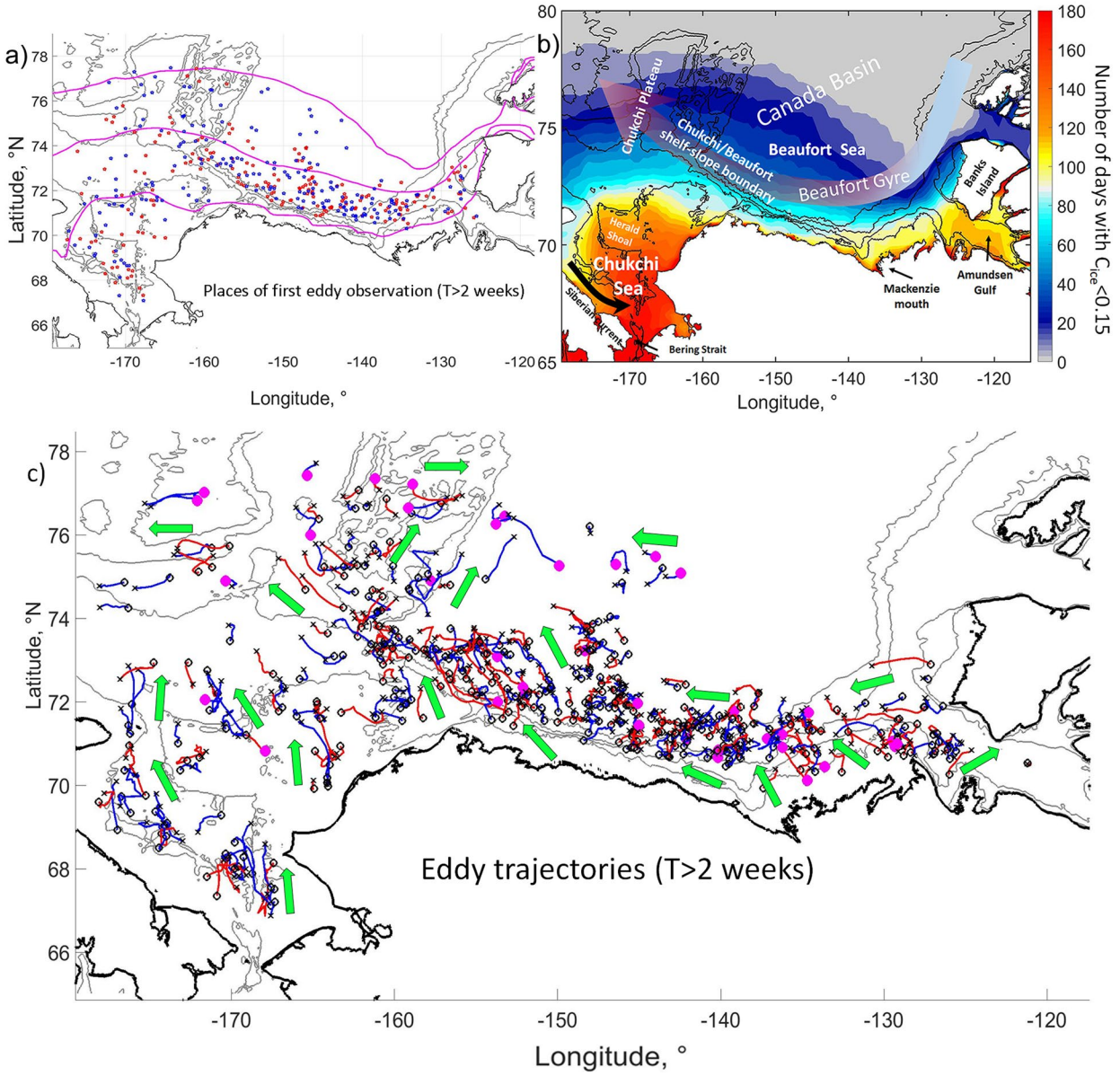

Figure 5. (a) Locations of the first eddy encounter in the gridded altimetry data for eddies with period of eddy observations $T > 5$ days, pink lines show isolines of days per year with ice concentration $C_{ice} < 15\%$ (10, 30, and 90 days); (b) the average number of days per year with ice concentration $C_{ice} < 15\%$ based on MERRA-2 reanalysis for 1993–2019, large arrow shows a schematic direction of the BG; (c) trajectories of eddies with $T > 2$ weeks. Red color marks anticyclones; blue—cyclones. Crosses mark start positions of eddies, circles—their end positions. Green arrows show the dominant eddy translation directions. Pink markers show the eddies with a maximum radius of more than 45 km.

Maps of average eddy orbital velocities, V_{max}, and period of observations, T, are shown in Figures 7b and 7c. The most intense eddies with V_{max} = 0.15–0.20 m/s are observed on the Chukchi/Beaufort shelf-slope boundary (region 3). This position and velocity values closely correspond to the characteristics of the large-scale currents of the BG that are most intense over this region (see Figure 6a). Since eddies are presumably formed along the large-scale boundary currents and interact with them during their lifetime, their velocities should have similar values. In this region, eddies are also characterized by a long period of observations exceeding two weeks (Figure 7c).

Zone of the longest period of observation ($T > 30$ days) and rather intense orbital velocities of 0.12–0.2 m/s of eddies extends from the Mackenzie River mouth to the northwest. Such distribution suggests that the baroclinic effects due to the Mackenzie River plume (see Section 4.2) likely play an important role in the

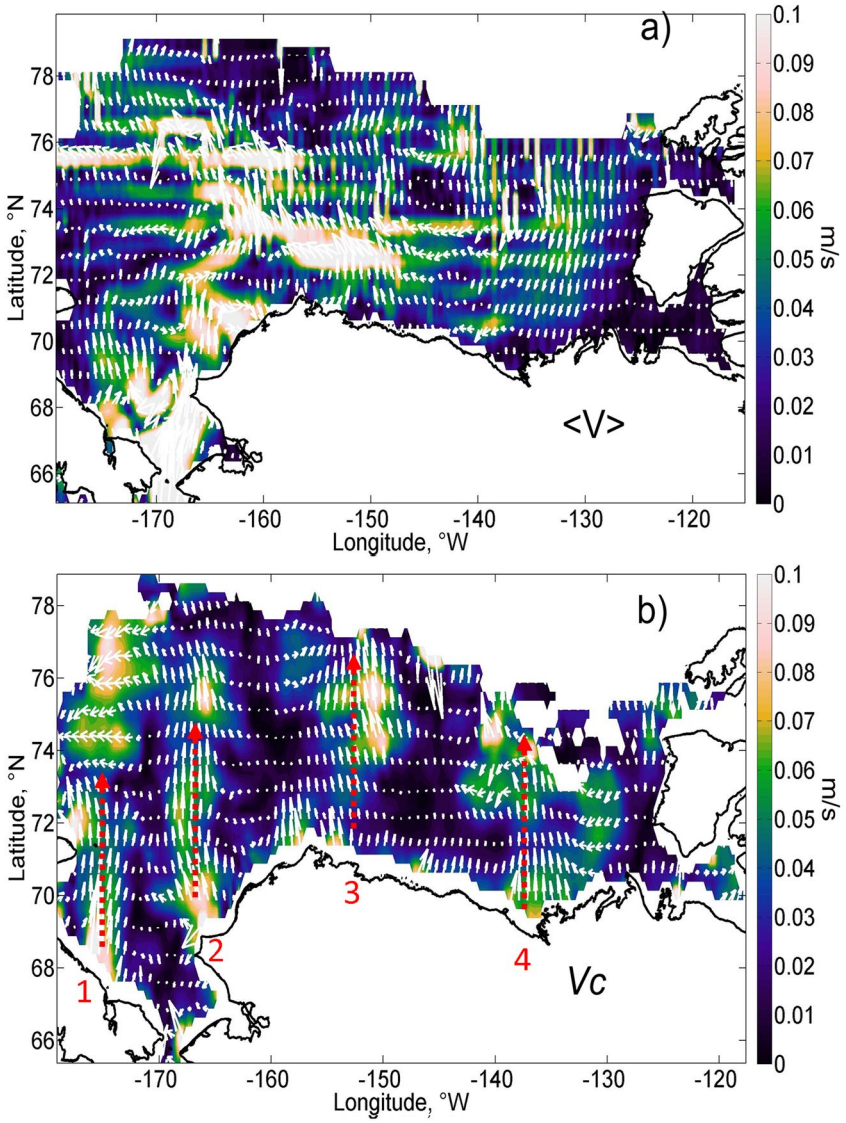

Figure 6. Average over 1993–2016 map of (a) geostrophic current velocities (m/s), (b) eddy translational velocities (m/s). Red arrows in (b) show the longitudinal bands where eddies propagate poleward.

generation of intense eddies over the basin. The orbital eddy velocities are the smallest in the north-eastern BS west of Banks Island.

Another area of high V_{max} (>0.2 m/s) is located in the western CS. It extends along the coast and is located to the north of the Siberian Coastal Current. Relatively high velocities are also observed in the north-eastern part of the CS along the Alaskan Coastal Current. At the same time, the eddies detected in the southeastern CS and north of the Bering Strait are characterized by minimal T values that are probably related to the shallowness of the basin. This agrees with the SAR observations showing a relatively small number of eddies in this area (Kozlov et al., 2019).

The distribution of time-averaged eddy-induced vorticity Ω shows the presence of an asymmetry in the geographical cyclone/anticyclone formation (Figure 7d). Larger negative vorticity values indicating the dominance of AEs are observed along the Chukchi/Beaufort shelf-slope boundary. This may be related to the anticyclonic shear on the inner periphery of the large-scale BG currents indicating the importance of this mechanism for the formation of AEs. At the same time, cyclonic eddies are dominant in the northernmost

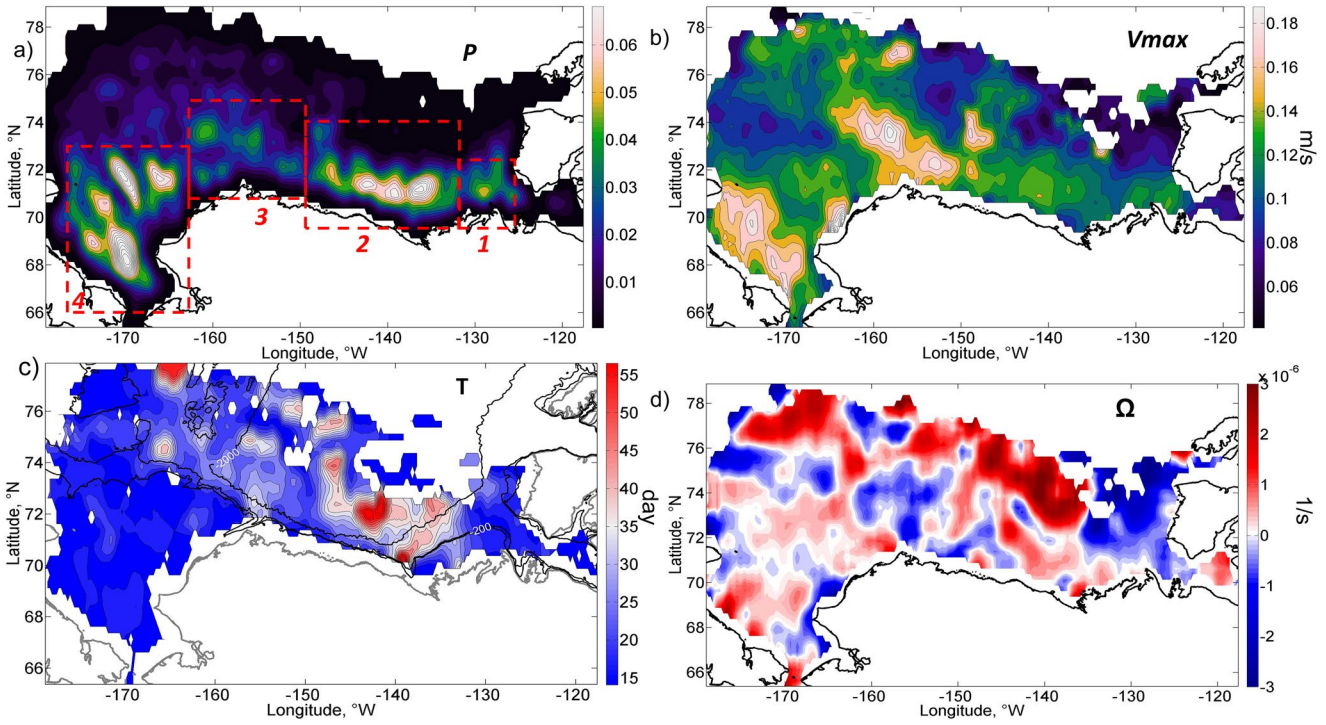

Figure 7. Average over 1993–2018 distribution of eddy properties defined in Section 2.1: (a) eddy probability P; (b) maximal orbital velocity V_{max} (m/s); (c) period of eddy observations T computed using 7-day averaged altimetry maps (day); (d) vorticity Ω (1/s). Dashed red boxes in (a) mark four regions of enhanced eddy activity described in more detail in Section 4: (1) the Amundsen Gulf, (2) the Mackenzie River plume, (3) the western Beaufort Sea, (4) the CS. White color in the northern parts of all maps marks ice-covered regions with no information on eddy properties available.

regions of the central BG. In the CS, cyclones dominate in the northern and western part of the basin, while anticyclones dominate in its eastern part.

The number of detected eddies in the particular region depends on the region size and the percentage of the ice-free areas over them. The CS is the largest region and the Amundsen Gulf is the smallest. A maximum number of eddies was detected in the largest region—the CS (region 4) with a peak of 19 eddies in October (Figure 8a). In regions 2 and 3, the seasonal peak in the number of identified eddies was observed in September with 16 and 13 eddies detected per month, respectively. The minimum number of eddies was observed in the Amundsen Gulf, which had an almost equal number of eddies throughout the season with small peaks in June and October.

Because sea ice represents an obstacle for SSH measurements with altimetry, the eddies in the study region are detected mostly during the ice-free season from April to December (Figure 2d). The seasonal variability of eddy-covered ice-free area S shows that regions 2 (the Mackenzie River plume) and 3 (the western BS) experience the maximum values of S in September, while for the CS (region 4) it occurs later, in October–November (Figure 8b). In the Amundsen Gulf (region 1), two peaks are detected—in June and September. The largest S is obtained in region 2.

The eddy statistics concern only the ice-free season when altimetry data are available. However, the observed timing of the seasonal peaks coincides well with the results from year-round observations (Manley & Hunkins, 1985). The decrease in the number of eddies in the cold period of a year has previously been attributed to the impact of ice friction and the absence of direct atmospheric forcing (Manley & Hunkins, 1985; Meneghello et al., 2020).

The number of detected eddies and the eddy-covered area generally have similar interannual variability with distinct regional features (see Figures 8c–8f). In the small Amundsen Gulf, no eddies were detected in 1996–1997, 2002, 2008, 2012–2013, while in other years on average two eddies were detected (Figure 8c).

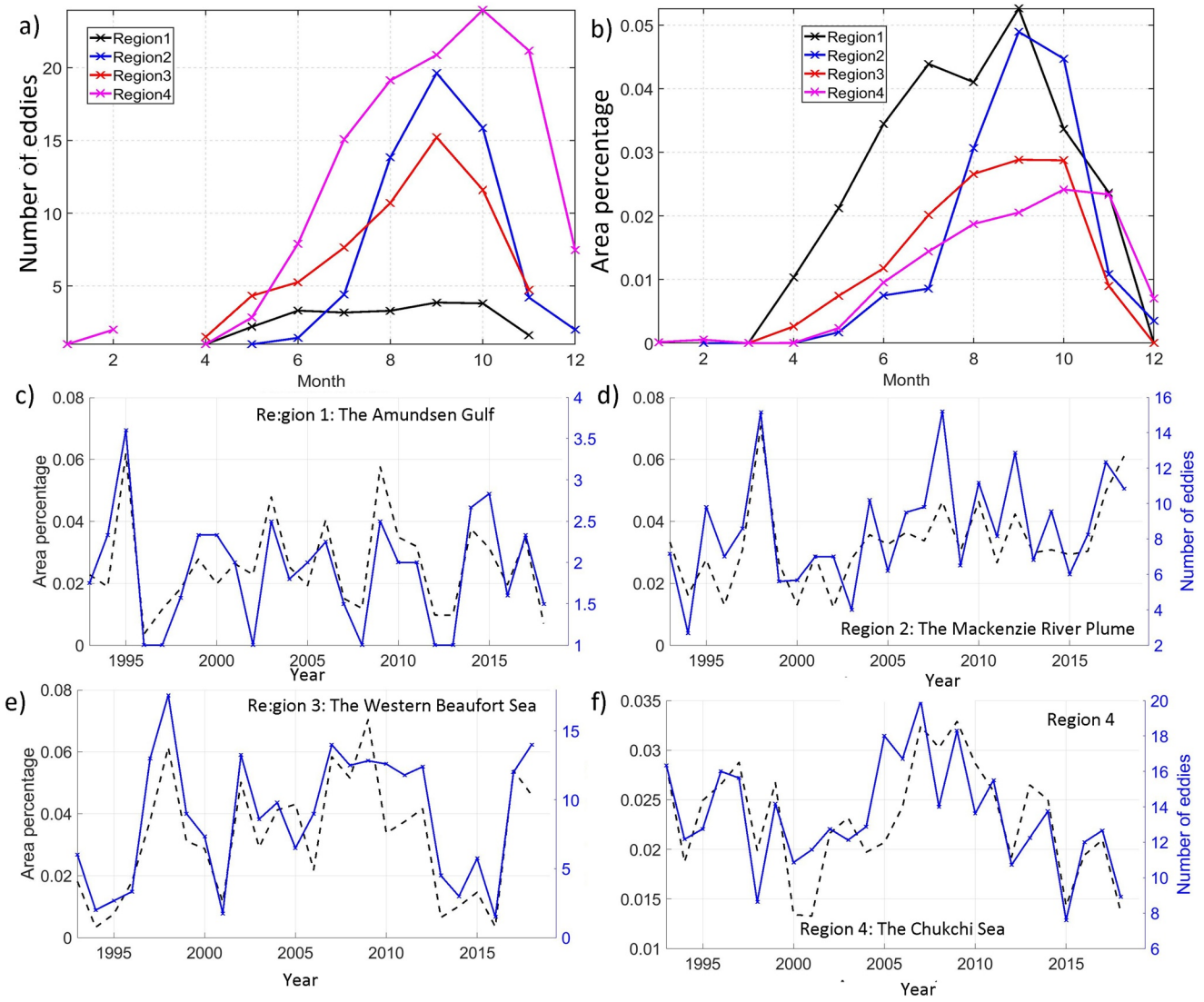

Figure 8. (a and b) Seasonal variability of (a) the number of eddies identified in the ice-free ocean and (b) the percentage of area occupied by eddies relative to the total area with available altimetry measurements *S*; (c–f) interannual variability of the yearly averaged *S* (black dashed line) and the number of identified eddies in the ice-free ocean (solid blue line) in regions 1–4 marked in Figure 7a.

Several coinciding peaks are observed in regions 2 and 3 (Figures 8d and 8e). The first peak is observed in 1998 and is probably related to the sharp increase of Mackenzie River discharge (see Section 4.2). In region 3, another two maxima are observed–in 2002 and during 2006–2012. These maxima are followed by the minima found in 2013–2016 and the increase in eddy number seen during recent years (2017–2019). A similar minimum in 2013–2016 and an increase in 2017 are observed in region 2. In the CS (region 4), the highest number of eddies is detected in 2004–2009 between two minima found in 1999–2003 and 2012–2018 (Figure 8f).

4. Regional Features of Eddy Dynamics in the Western Arctic

4.1. Region 1. The Amundsen Gulf

Mesoscale eddies were frequently detected at the entrance to the Amundsen Gulf between Banks Island and the Canadian coast (see Figures 5a and 7a). An eddy found in this location was recently described by Sévigny et al. (2019) using thermal MODIS data and oceanographic measurements made in 2004. This eddy, with a radius of 20 km, was characterized by a 15 cm anomaly of dynamic height and had a strong impact

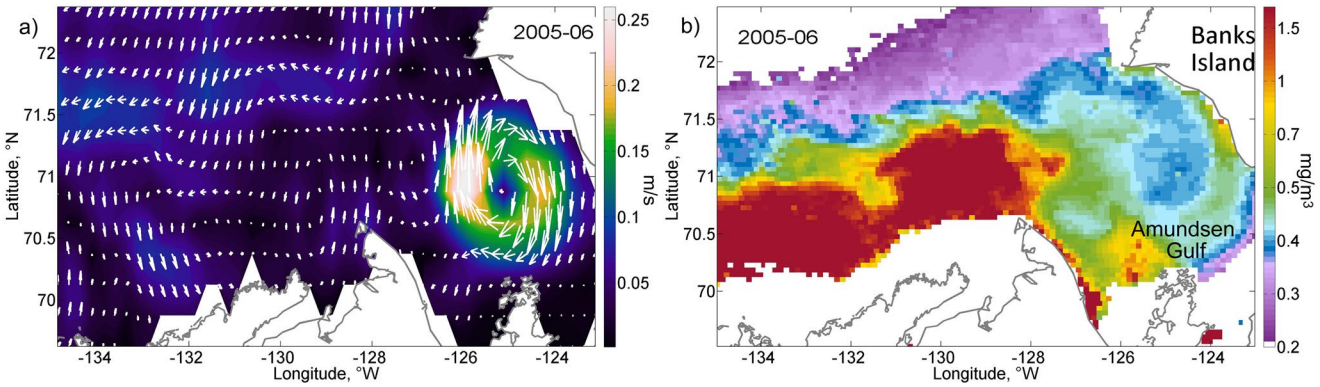

Figure 9. Quasi-stationary anticyclone at the entrance to the Amundsen Gulf in the monthly averaged (a) altimetry-derived geostrophic velocity (m/s) and (b) MODIS chl-a concentration (mg/m^3) in June 2005.

on the vertical transport of heat over this area (Sévigny et al., 2019). Our analysis shows that a similar eddy, sometimes accompanied by several smaller eddies, usually occupies the entire entrance to the gulf and has a diameter comparable to the entrance width. For example, an anticyclonic eddy at the gulf entrance is well observed in the map of average geostrophic circulation for June 2005. Its velocity reaches 0.25 m/s and the radius is about 50 km (Figure 9a). This eddy is also well expressed in MODIS chl-a data for the same month (Figure 9b). The eddy traps the deep Arctic waters that are low in chl-a from the north toward the gulf center and pushes the shelf waters with high chl-a values northward in the western part of the strait. In some years, for example, in 2005, this large anticyclone was observed in MODIS data throughout the entire ice-free season from June to November.

Analysis of satellite data confirms that this eddy is quasi-stationary. Most of the time, it is anticyclonic, but sometimes a cyclonic eddy is formed in this zone as well. An example shown in Figures 10a and 10b demonstrates the presence of an AE at the gulf entrance on September 10, 2015 and a CE on September 9, 2016 in MODIS SST data. In both cases, the eddy entrains the cold Arctic waters into the gulf where the water temperature is two degrees higher. In the first case, the eddy entrains cold Arctic waters from the north at its eastern periphery, while in the second one the entrainment occurs at its western periphery.

The location of this eddy suggests that its dynamics are related to the dynamics of the strait and the Amundsen Gulf. Similar eddies are formed in the Alboran Gyre near the Strait of Gibraltar (Ovchinnikov et al., 1976; Whitehead & Miller, 1979), where the eddy is generated as a result of episodical inflow of the light Atlantic waters over the dense Mediterranean Sea waters caused by tidal or wind forcing. This mechanism is described in detail in a laboratory experiment by Whitehead and Miller (1979). In our case, a similar mechanism may be responsible for the eddy formation in this region.

However, as the Amundsen Gulf is shallow, barotropic forces may be of greater importance here. The intensity of the barotropic inflow in the relatively shallow Amundsen Gulf can be significantly modulated by wind surges. According to the altimetry data, northerly winds can intensify the southwestward currents along the Banks Island (see an example in Figure 10a). Such currents cause the inflow of cold waters of the central Arctic in the Amundsen Gulf along the Banks Island, which pushes light waters from the gulf and induce an anticyclonic rotation (Figure 10a). Indeed, such AEs were mostly observed during the months when northerly winds were dominant over the entrance to the Amundsen Gulf, for example, in June 2005 or September 2015 (Figure 10c). At the same time, CEs were usually generated in opposite situations, when southerly winds blew, as in September 2016 (Figure 10d). Such wind conditions probably cause the northward flow of the gulf waters along the Banks Island in the eastern part of the gulf, which is compensated by the inflow of cold deeper waters in its western part (see arrows in Figure 10d).

Analysis of the wind variability at the entrance of the Amundsen Gulf during the ice-free period shows that northerly winds usually dominate here in the summer period (see the wind rose in the upper-left corner of Figure 10b), which promotes the generation of AEs. Southwesterly winds directed out of the gulf are often

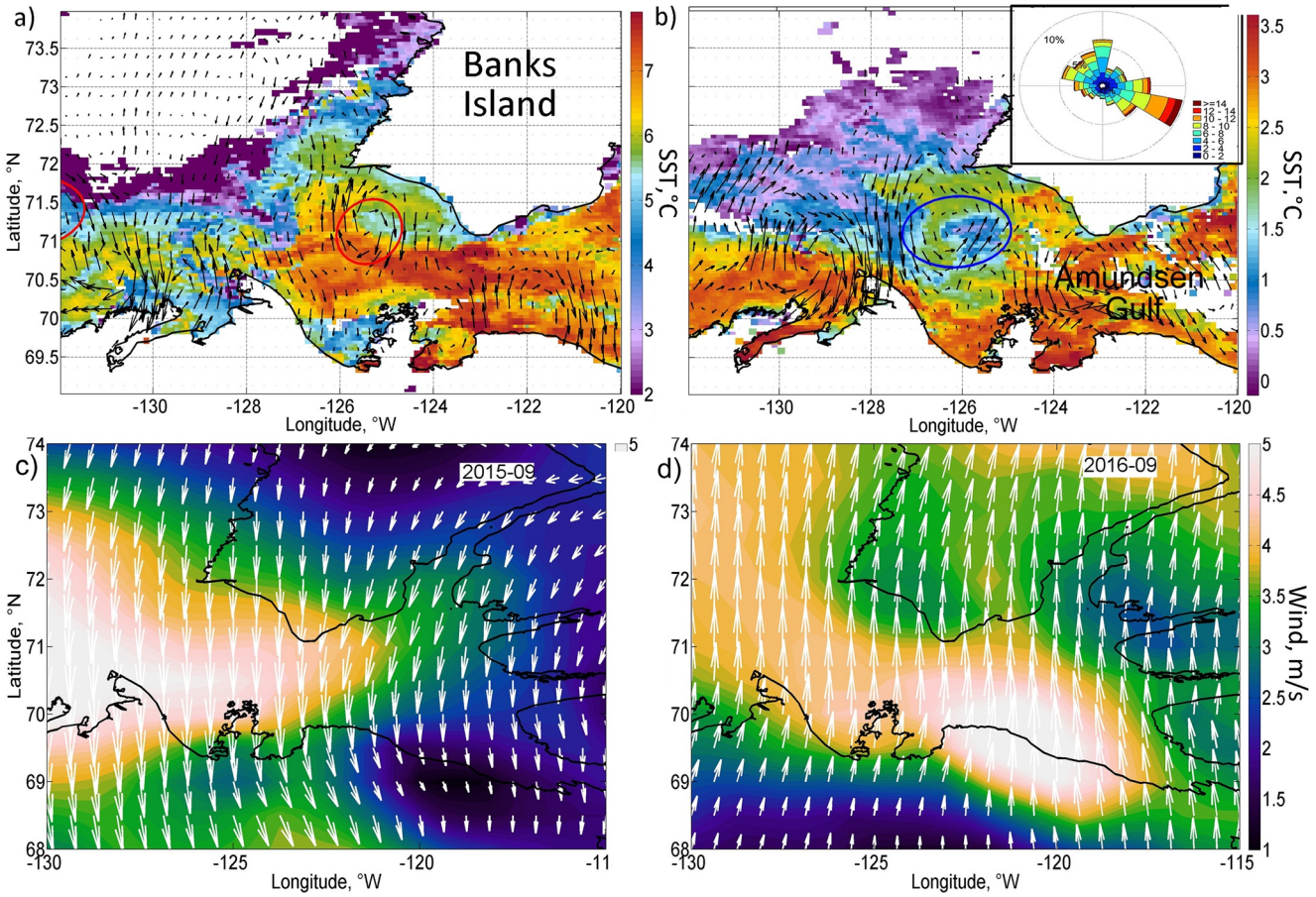

Figure 10. An example of anticyclonic (a) and cyclonic (b) eddies formed at the entrance to the Amundsen Gulf on September 10, 2015 and September 30, 2016, respectively, as observed in MODIS SST and altimetry data. Black arrows show altimetry-derived anomaly of geostrophic velocity. Red and blue ellipses show the position of the identified eddies. A small image in the upper-left corner of (b) shows the wind rose for the point 70°N and 126°W at the entrance to the Amundsen Gulf. (c and d) Monthly averaged MERRA-2 wind maps (m/s) for September 2015 (c) and September 2016 (d).

observed here in autumn and can be very intense, above 15 m/s (Figure 10b), promoting the generation of CEs.

4.2. Region 2. The Mackenzie River Mouth

The second discussed region is located north-west of the Mackenzie River mouth. It extends westward and then at 145°W elongates to the northwest. The most likely mechanism of eddy generation in this region appears to be baroclinic instability of the front of the river outflow plume (Mulligan & Perrie, 2019). The overflow of the warm and brackish plume waters onto the cold and saline ocean water induces the formation of mesoscale anticyclones that are observed in this region more often than cyclones (see examples in Figures 3, 11a and 11b). Density gradients between the plume and the cold open ocean are largest in May–June during the peak of the Mackenzie River discharge (Yang et al., 2015). The associated buoyancy gradients can generate intense anticyclonic geostrophic frontal currents around the plume area. Horizontal shear on this boundary current and the periphery of large mesoscale anticyclones can cause barotropic instability and the formation of eddies of different signs on the plume front.

An example of the generation of such eddies was already demonstrated in the MODIS data shown in Section 2, where Figure 3 showed the Mackenzie River plume evolution during a week in July 2008. Several anticyclones and cyclones are present on the offshore border of the plume. Both cyclones and anticyclones entrain the plume waters in their orbital movements and transfer it to the north, providing a cross-front mixing of the plume and the deeper waters of the central Arctic basin, which have low values of chl-a.

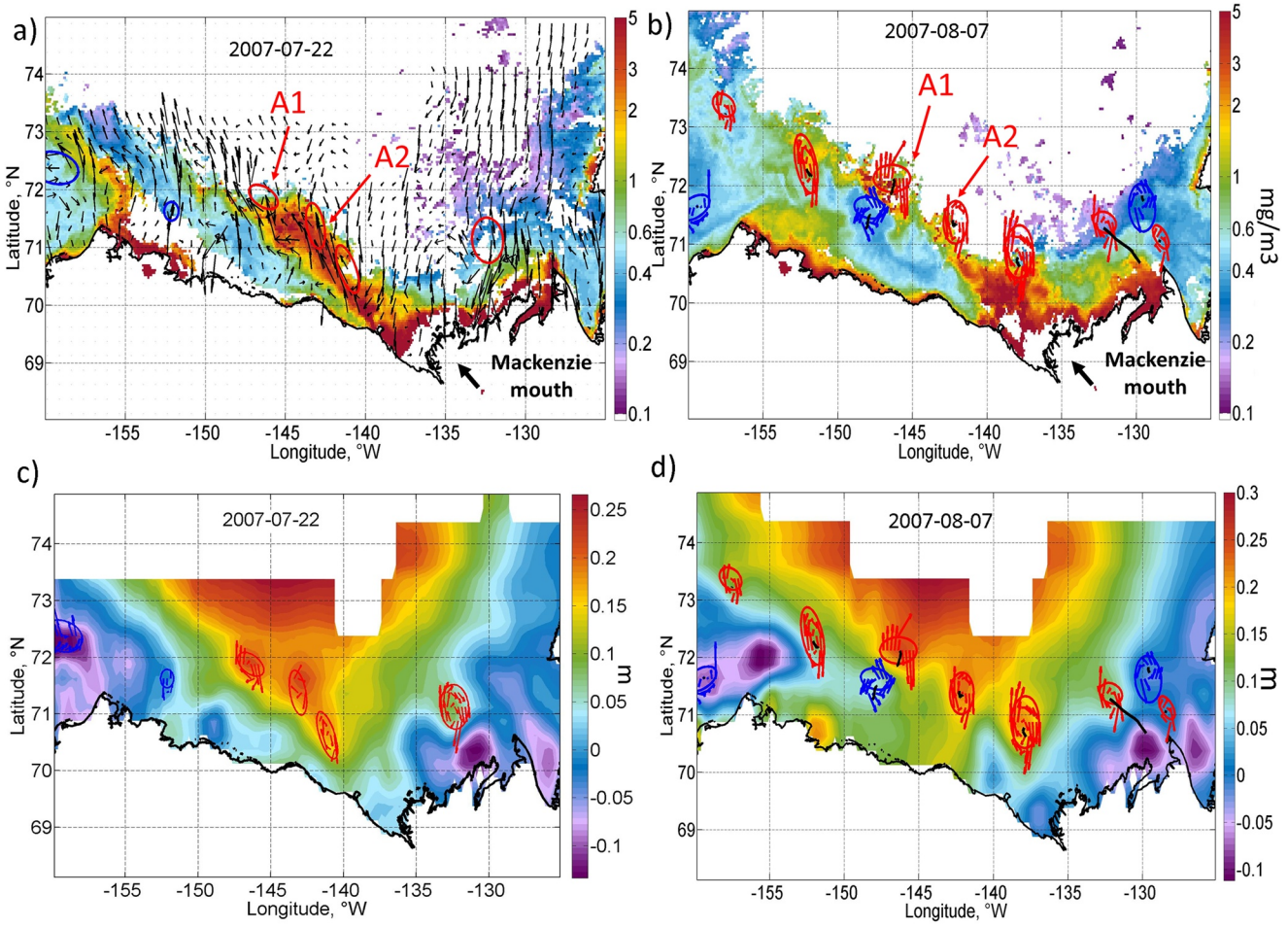

Figure 11. Eddies identified in altimetry data superimposed on (a) 8-day averaged MODIS Aqua chl-a concentration map (mg/m^3) centered on July 22, 2007; (b) 8-day averaged MODIS Aqua chl-a concentration map centered on August 7, 2007; (c and d) altimetric sea level distribution (m) on (c) July 22, 2007 and (d) August 7, 2007. Black arrows in (a) show the altimetry-derived geostrophic velocities. Red ellipses show anticyclones, blue ellipses—cyclones. Black lines in (b–d) show eddy trajectories.

The Ekman transport associated with upwelling-favorable easterly winds (Kirillov et al., 2016) transfers the plume water further offshore to the north (Carmack & Kulikov, 1998; Mulligan & Perrie, 2019; Pickart et al., 2013). The plume and its frontal border displace northward, which is clearly observed in the consecutive 8-day averaged MODIS images shown in Figure 3. Further, anticyclonic currents of the BG prevailing over the continental slope transport the plume water westward (Figure 3b). As a result of these processes, the plume moves in the northwestward direction.

Another example of such a plume displacement is observed in MODIS imagery in July–August 2007 (Figures 11a and 11b). The band of the plume water enriched in chlorophyll extends from the Mackenzie River mouth to the northwest on July 22, 2007 (Figures 11a and 11c). Three anticyclonic eddies attached to the plume are also found northwest of the mouth. Two weeks later, the plume has moved further northwest, and waters that are high in chl-a reached 155°W on August 7, 2007 (Figure 11b). Several more eddies have formed on the plume periphery in the western part of the basin. Eddies A1 and A2 slowly displaced to the northwest by this time. Particularly, the center of A1 has moved on about 20 km to the northwest crossing the 72°N latitude.

The salinity anomaly in the plume water can strongly affect the thermohaline and dynamic structure of the central BS (Nghiem et al., 2014). On the altimetric maps for June and July 2007, the positive SLA related to the plume is close to its value in the central part of the BG (Figures 11c and 11d). Such a rise in the sea level can cause a noticeable intensification of the anticyclonic vorticity in this area. Geostrophic velocities

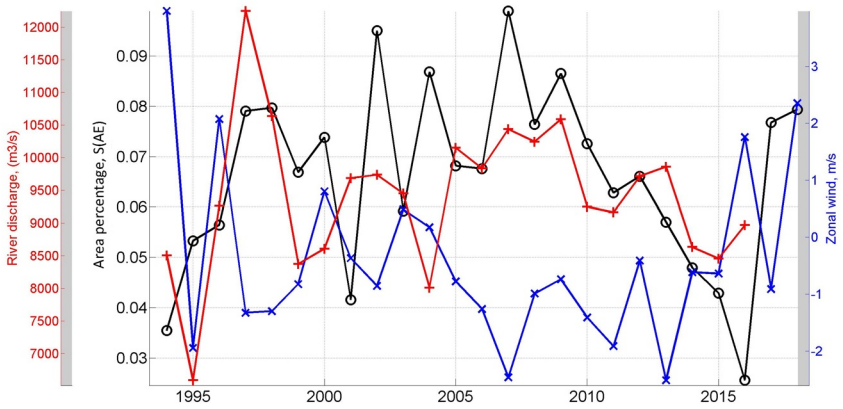

Figure 12. Average annual variability of the percentage of area occupied by AEs (black line) in region 2 near the Mackenzie River mouth, Mackenzie River discharge (red line, m^3/s), and the zonal wind velocity (blue line, m/s) at the point (74°N, 134°W).

also clearly depict the buoyancy-driven anticyclonic circulation rounding the plume in Figure 11a. In the time-averaged map of geostrophic velocity, this anticyclonic pattern of circulation is also seen, at 145–155°W longitudes (Figure 6a). Currents in this area are directed northward, creating another short branch to the center of the BG (Figure 6a). This current can explain the intense northward migration of the eddies observed in this area in Figure 6b (arrow 4).

The generation of eddies through this mechanism is related to the intensity of the interaction between the light plume water and the deeper and denser Arctic water. This process depends, first, on the river discharge, which modulates the amount and salinity of the plume water. Second, it depends on the offshore propagation of the plume to the deep part of the basin. The propagation is modulated by the upwelling-favorable easterly winds (Carmack & Kulikov, 1998; Mulligan & Perrie, 2019; Pickart et al., 2013) and the intensity of the BG.

Figure 12a shows the annually averaged variability of *S*(AE) in region 2. More eddies are usually observed in the years with high river discharge (red line in Figure 12). A maximum of *S*(AE) in 1998 coincides with the sharp rise of the Mackenzie River discharge during this year (Yang et al., 2015). An increase of river discharge was also observed in 2007–2009 when the absolute maximum of eddy activity was detected.

Comparison of time variability of *S*(AE) with wind characteristics shows that *S*(AE) is also negatively correlated with the zonal wind (blue line in Figure 12). Before the wind averaging, we exclude wind data for the ice-covered periods, when no eddies could be detected. Upwelling-favorable anticyclonic winds (with the negative easterly component along the coast) cause the offshore displacement of the plume and its overflow on the dense, deep waters leading to enhanced generation of AEs. Such winds also intensify the anticyclonic BG, which promotes the plume displacement to the west and increases the horizontal shear and related instabilities. Strong anticyclonic circulation observed in summer 2007–2008 is one of the probable reasons for the peak of both area and number of AEs in that year. In particular, 15 unique AEs were detected in altimetry data in July 2007 over this region. The year 2007 was also characterized by the minimum ice cover extent that also should give a contribution to the observed peak in the number and area of AEs.

A minimal number of eddies is observed during the intensification of westerly winds. Such winds press the plume to the coast, move it eastward and suppress the formation of large eddies that can be detected in altimetry data over the study region. Such a situation was observed, particularly, in the summer seasons of 1994 and 2016, explaining the observed minima in the number of AEs (Figure 12).

4.3. Region 3. The Western Beaufort Sea

Another key region of eddy observations is found in the western BS on the Chukchi/Beaufort shelf-slope boundary along the pathway of the northwestward flowing currents of the BG. The examples in Figures 13a and 13b demonstrate the intense mesoscale dynamics in the western BS in the altimetry data and the

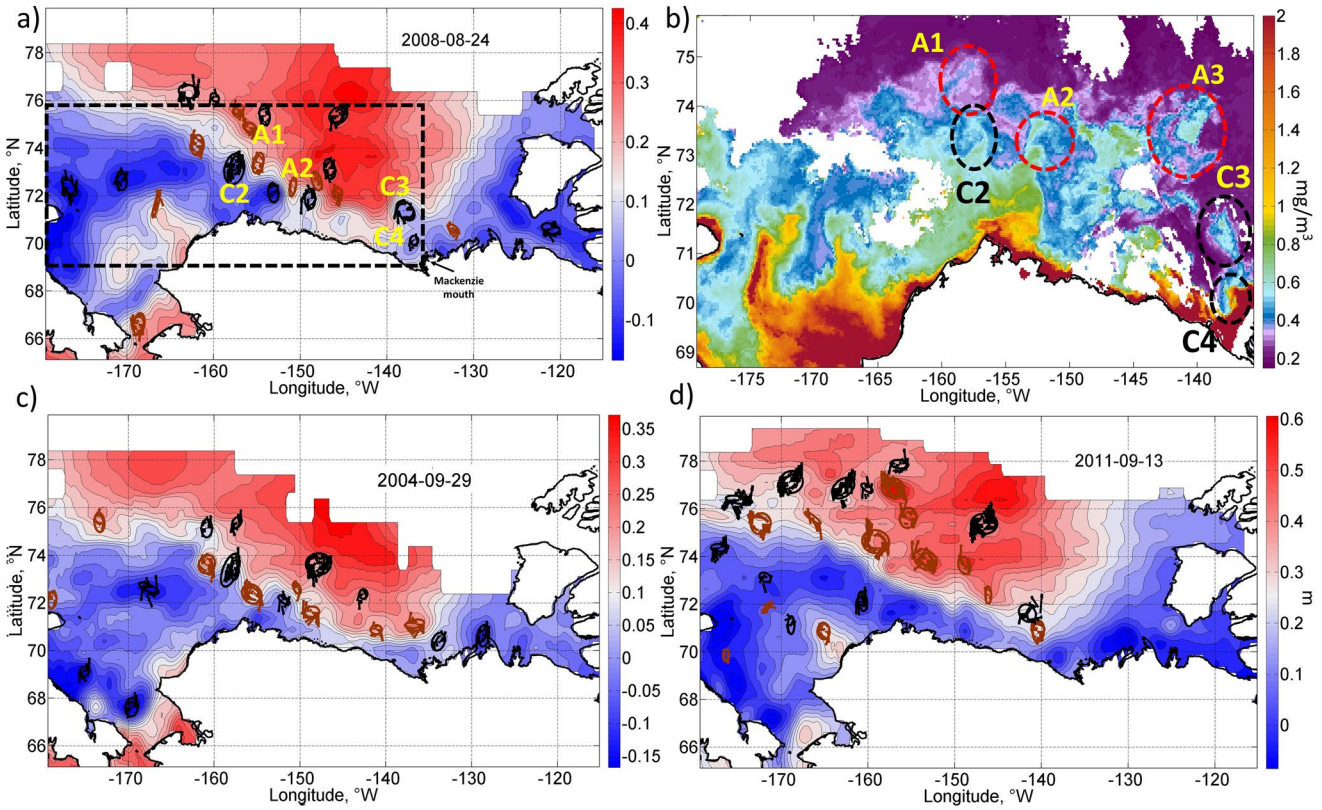

Figure 13. Identified eddies (blue—cyclones, red—anticyclones) superimposed on the altimetry-derived dynamic topography (m) for (a) August 24, 2008; (c) September 29, 2004; (d) September 13, 2013. (b) Zoomed MODIS chl-a map (mg/m^3) for August 24, 2008 (black rectangle in (a). Red (black) circles in (b) show the approximate position of anticyclones (cyclones) identified in altimetry data.

MODIS chl-a map on August 24, 2008. Waters with a high chl-a concentration of 0.6–0.7 mg/m^3 occupy a large area in the southwestern BS. These waters appear to trace the propagation of the nutrient-rich Pacific-origin water toward the deep regions of the basin. Several mesoscale eddies are present in the field of chl-a tracers between the regions of coastal waters with high chl-a (>0.5 mg/m^3) and low chl-a (<0.2 mg/m^3) of the deeper Arctic basin. These eddies trap waters with a high chl-a from the south and transport them further into the deep Canada Basin, illustrating the importance of eddy lateral advection in fueling the deep Arctic Ocean with nutrients (see e.g., Watanabe, Onodera, et al., 2014). These eddies are very densely packed, so it is hard to distinguish all of them on the chl-a map. However, some of them are well seen. For example, cyclone C2 and anticyclones A1–A3 in the northern part of this map transport high chl-a waters to the north up to 74.5°N about 100 km northward from the main front, the distance comparable to the diameter of these eddies. Other distinct features to be mentioned here are the cyclones C3, C4 found north of the Mackenzie River mouth. The eddies C1–C3, A1–A2 are well-identified by altimetry data, but the eddy A3 was not detected (Figure 13a). At the same time, the altimetry data have revealed several eddies in the northernmost parts of the region, where chl-a gradients are low. Three cyclones and two anticyclones are observed near the Chukchi/Beaufort shelf-slope boundary at 75–76°N.

The altimetry-derived geostrophic currents are maximal (>0.1 m/s) in the southwestern part of the BG at longitudes 145–155°W and further extend to the northwest up to 76°N, 170°W (Figure 6a). This part of the gyre is impacted by the Mackenzie River plume in the south, and the inflowing waters of Pacific origin coming from the southwest. The interaction between dense Pacific-origin and the light Canada Basin waters intensifies the current and its baroclinic and barotropic instabilities, which are the probable reasons of the intensification of eddy dynamics in this region (Corlett & Pickart, 2017; Spall et al., 2008). Frontogenesis (Capet et al., 2008) associated with the stirring of the two water masses due to the BG intensification/weakening can be another mechanism of eddy generation in this area.

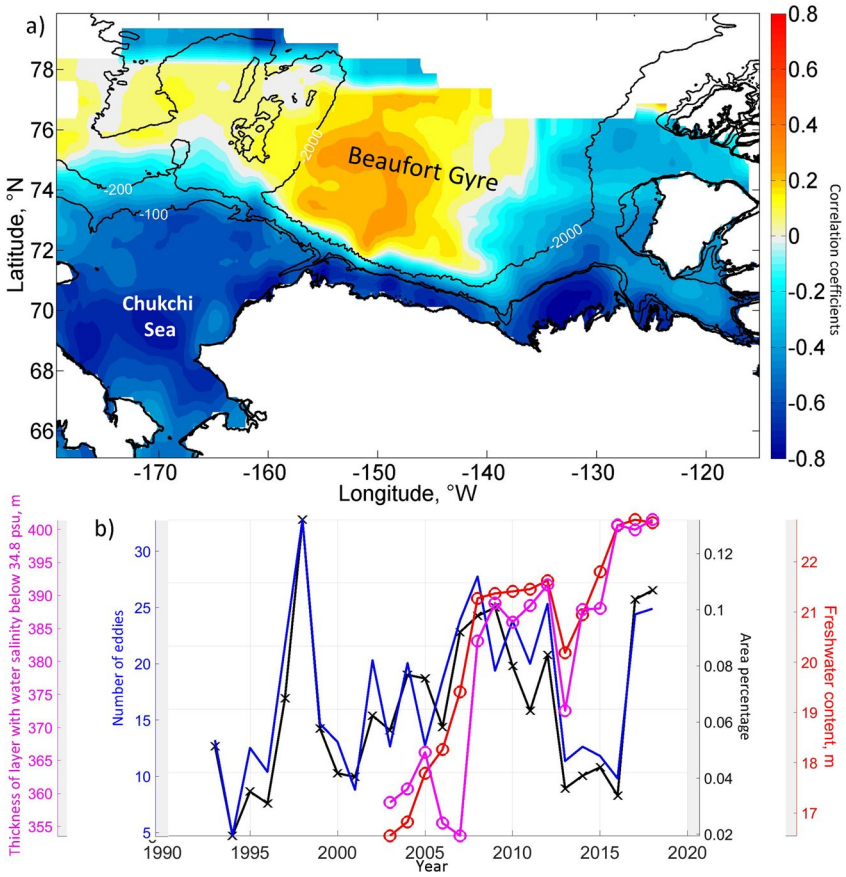

Figure 14. (a) Correlation map between the number of AEs on the Chukchi/Beaufort shelf-slope boundary in the western BS (region 3 in Figure 7a) and sea level variability smoothed by a 1-year moving average; (b) Interannual variability of the probability (black line), number of eddies (blue line) identified in regions 2 and 3, the estimates of freshwater content (FWC, m; red line) and thickness of layer with water salinity below 34.8‰ (m; magenta line) in the BG derived from ITP and mooring records presented in Proshutinsky et al. (2019).

Eddies are also frequently observed along the Chukchi/Beaufort shelf-slope boundary (Figures 13c and 13d), with over 10 large eddies typically appearing here in summer. Often cyclonic eddies were observed not only in the center of the gyre but also on its northwestern periphery (Figures 13a and 13d). Anticyclones are usually located closer to the continental slope, while cyclones are observed over the deeper Canada Basin, mimicking the mean vorticity field (Figure 7d). This suggests that horizontal current shear in the BG flanks could be important for eddy generation and sign. The interannual variations of the BG strength and horizontal extent are in part correlated with the changes in eddy locations. For example, the relatively small and weak BG, having its easternmost center location in 2004 (Regan et al., 2019), co-occurred with the eastward shift of the eddy field (Figure 13c). In contrast, a clear intensification and westward expansion of eddies were observed during the BG intensification in 2011 (Figure 13d).

There is a well-defined correlation pattern between S(AE) and SSH variability, with the positive correlation of 0.2 in the center of the gyre and the negative correlation of −0.7 on its periphery and in the CS (Figure 14). This suggests that the intensification of the anticyclonic BG circulation, which increases sea level in the center of the basin and decreases over the slope, plays a major role in the interannual eddy variability. The border between the zones of positive and negative correlation is located exactly along the Chukchi/Beaufort shelf-slope boundary. The magnitude of the negative correlation over the continental slope is significantly higher than the positive values in the center of the basin, indicating that upwelling over the shallow areas is a more efficient indicator of eddy generation in this area. Intensification of the BG not only increases horizontal shear but also promotes advection of the light Mackenzie River plume waters, which contribute to the rise of the current strength and its baroclinic instability. As the upwelling-favorable

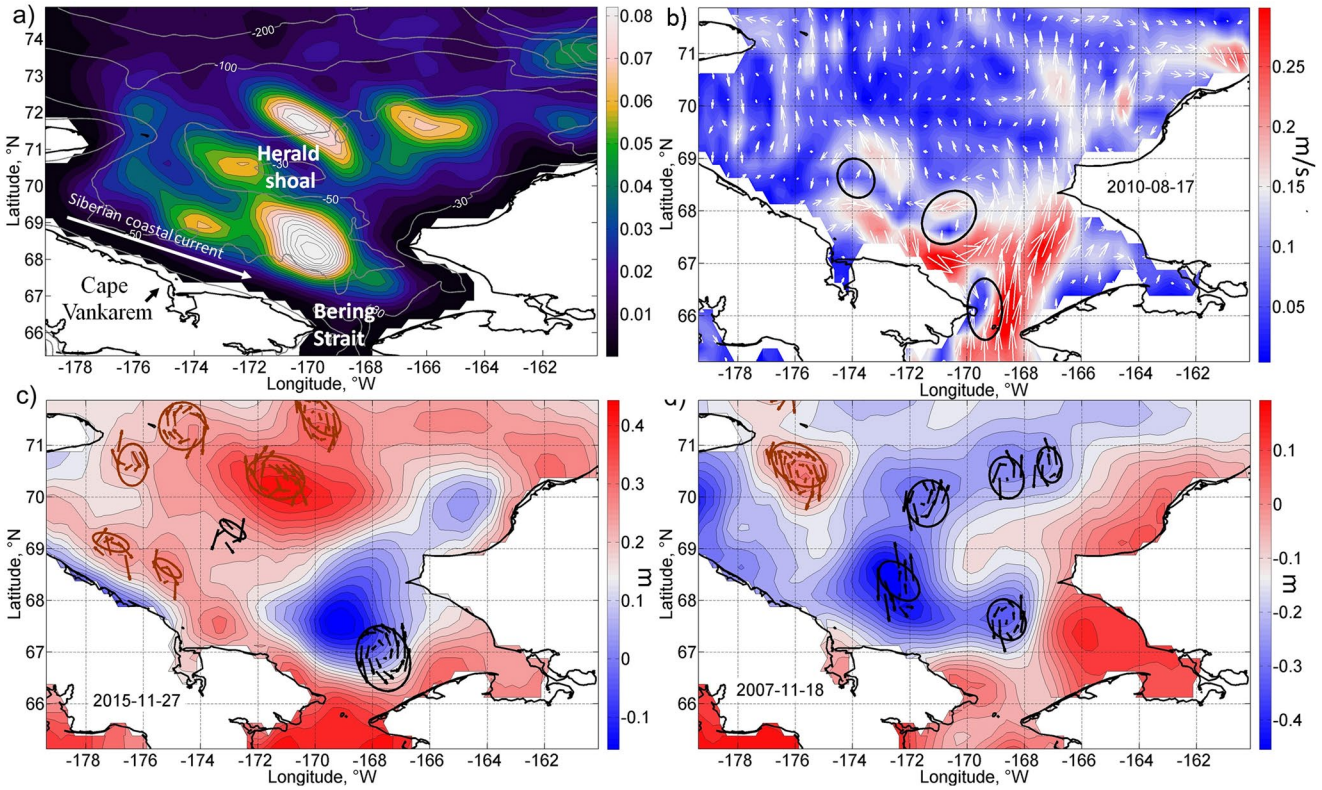

Figure 15. (a) Average distribution of altimetry-derived eddy probability in the Chukchi Sea. Black lines mark isobaths; (b) Example of altimetry-derived geostrophic currents (m/s) and identified eddies in the Chukchi Sea on August 17, 2010; (c and d) Examples of altimetry-derived dynamic topography (m) and identified eddies on November 28, 2015 (c) and November 18, 2007 (d).

anticyclonic winds are the main driver of the BG acceleration, the time variability of the eddy statistical characteristics in regions 2 and 3 have several similar features (Figures 8d and 8e).

An intercomparison of the area and the total number of eddies identified in regions 2 and 3 with estimates of freshwater content (FWC) in the BG (Proshutinsky et al., 2019) demonstrates their relation (Figure 14b). The increase in the number of eddies in 2005–2008, followed by their relatively constant number in 2008–2012, is in good agreement with the FWC behavior. In 2013, the FWC declined and then rose back nearly to 22 m in 2015. The altimetry data show a pronounced decrease in the number of eddies during this period, which then was followed by the rise in 2017–2018, coinciding with the increase of FWC. Apart from having a pronounced drop in 2007, the interannual variability of the thickness of layer with water salinity below 34.8‰ is also similar to that of the FWC and also has some correlation with the number of eddies identified in regions 2 and 3. However, the major difference is that the FWC is characterized by an intense positive trend, while the number and area of eddies remain almost constant. Such a trend in salinity may be related to climatic changes in stratification that do not significantly affect the BG strength. This indicates that the gyre circulation defined by sea level gradients (Figure 14a) rather than its thermohaline properties is the better predictor of the eddy intensity.

4.4. Region 4. The Chukchi Sea

The CS has several hot spots of eddy occurrence. The highest eddy activity is observed in its southern part north of the Bering Strait, north of Cape Vankarem (the Russian Chukotka coast), and in its central part northeast and west of Herald Shoal (Figure 15a). The detected eddies are mostly short-lived, consistent with rapid dissipation by benthic friction. The maximum eddy number in this region is detected by the altimetry data in late autumn, that is, in October–November (Figure 8a).

According to the altimetry data, one of the reasons for the eddy generation in this region is related to the Siberian Coastal Current flowing along the Russian coast. This current is characterized by intense interannual variability and can change its direction from eastward to westward (Weingartner et al., 1999). During the period of eastward flowing currents, the horizontal shear on its offshore flank may lead to the generation of the number of cyclonic eddies, which then move to the southeast, as shown in an example for August 2010 (Figures 15b and 15d). In contrast, during its westward flow (see, e.g., in November 2015; Figure 15c), series of anticyclonic eddies are generated. Figure 15c exhibits at least three AEs along the Russian coast, two of which are properly identified by our algorithm.

The maximum eddy activity north of the Bering Strait is probably associated with the strait dynamics. The Pacific-origin water entering the strait rotates cyclonically and sometimes forms an eddy-like structure in this part of the basin. Such cyclonic structures are seen in all three examples shown in Figures 15b–15d and correspond to the maximum eddy probability seen in the southern CS in Figure 15a.

The maximum eddy occurrence found northwest of Herald Shoal (between 71°N and 73°N) is located exactly where two branches of the Pacific water, namely the western and the central branches (e.g., Spall et al., 2018) meet. The horizontal shear between these two currents, as well as an interaction of the light Pacific and the dense Arctic waters in this area, is the most probable reason for eddy formation. In particular, at least four AEs are seen to the north and northeast of the bank on November 28, 2015 (Figure 15c). In contrast, several CEs are seen to the west and north of the bank on November 18, 2007 (Figure 15d). Such changes in the number and the sign of eddies are presumably related to the high variability of currents in this area. Additionally, topographic-driven vorticity changes, as well as bottom friction (e.g., D'Asaro, 1988), can probably lead to the eddy generation to the west of Herald Shoal, where another eddy maximum is observed.

5. Summary and Discussions

Our study provides a comprehensive overview of the surface geostrophic eddies and an insight into their formation mechanisms based on over 2000 coherent eddies detected in satellite altimetry over the seasonally ice-free areas of the western Arctic Ocean. The eddy characteristics vary dramatically in space and time due to the differences in their formation mechanisms and interactions with topography, mean currents, winds, and sea ice. The four key regions of intensified eddy generation are found to be (i) in the Amundsen Gulf, (ii) along the continental slope in the southern BS with primary region found north-west of the Mackenzie Bay, (iii) over the western periphery of the BG on the Chukchi/Beaufort shelf-slope boundary, and (iv) over the inner and outer shelves of the CS and near Bering Strait. A peculiar feature of the eddy variability, which is well observed in both MODIS imagery and altimetry data, is the quasi-stationary eddy located at the entrance of the Amundsen Gulf (region 1). This eddy is observed during the entire ice-free season for several years, and its formation appears to be associated with the strait dynamics. The second region is the Mackenzie Bay, where the formation of eddies is significantly related to the baroclinic instability of the Mackenzie River plume. A high number of large intense eddies were detected in the western part of the BG (region 3). These eddies are observed up to the northern open water boundary at 78°N. Their location and sign are closely related to the position of the BG current on the Chukchi/Beaufort shelf-slope boundary, with anticyclonic eddies formed to the north of the current and cyclonic eddies in the central part of the gyre. Altimetry data also show numerous locations in the southwestern and northeastern parts of the CS and along the Alaskan coast where eddy orbital velocities exceed 0.15–0.20 m/s.

The eddy translational velocities are mostly poleward all over the study area, with an exception in local areas of the eastern BS, where it is aligned with the BG and directed to the southwest. Eddies mostly move from the continental slope northward to the deep part of the basin. The translational velocity is generally between 0.01 and 0.06 m/s with a statistical peak at 0.035 m/s. The poleward translational eddy velocities are highest in the regions of intense northward currents in the northwestern part of the BS and in the western and eastern parts of the Chukchi Basin, where they reach 0.08–0.10 m/s. High values of eddy translational velocity are also observed near the Mackenzie River mouth (0.05–0.07 m/s) and are probably related to the wind regime and the rapid offshore plume propagation during the period of intense river discharge in summer.

The altimetry-derived eddy radii peak at about 30 km, reaching 65 km in some rare cases (with the upper limit of 70 km set by the eddy identification algorithm). This value is significantly higher than the estimates of the R_i in the Western Arctic Ocean of 5–15 km (Nurser & Bacon, 2014). The existence of such large mesoscale eddies was episodically documented in several previous studies (Sévigny et al., 2015; Watanabe, 2011; Wood et al., 2015). However, the long-term (1993–2018) altimetry data covering the large ice-free regions of the Western Arctic has allowed us to identify 2,365 individual eddies, suggesting they are frequent at such high latitudes. Their sizes are larger than those documented from in-situ ITP data (Zhao et al., 2014) and spaceborne SAR data (Kozlov et al., 2019). Mechanistically, the eddy scales are not only associated with their formation processes that determine their baroclinic structure but also with the expected inverse energy cascade and barotropization (Smith & Vallis, 2001), although the barotropization is expected to be weakened by the peculiarities of the Arctic stratification (Zhao et al., 2016).

Our altimetry analysis of large-scale eddies with strong surface geostrophic currents reveals a roughly equal partitioning between cyclones and anticyclones. However, the time-averaged distribution of eddy vorticity shows the presence of an asymmetry in the geographical cyclone/anticyclone formation: anticyclones are predominant on the periphery of the BG while cyclonic eddies dominate in the northernmost regions of the central BG. The asymmetry is presumably related to the sign of the shear on the southward periphery of the large-scale BG, which seems to play an important role in defining the sign of the observed large mesoscale eddies. The cyclone/anticyclone asymmetry appears prominently in other types of eddy observations, with anticyclones being dominant in the interior of the ocean observed via ITPs and moorings (Timmermans et al. 2008; Zhao et al. 2014, 2016), while surface eddy footprints as seen from SAR data appear to favor cyclones (Kozlov et al., 2019). These differences may be attributed to the fact that different observational methods are biased toward particular aspects of the complex eddy field: ITPs and moorings reveal the interior eddy field, SAR measurements their surface expressions, while altimetry only detects the large-scale eddies.

The interannual variability of the eddy probability shows clear peaks over selected periods in 1998–1999, 2008–2009, 2012, 2017–2018. For regions 2 and 3, this is similar to the ITP-based statistics on small-scale eddies encountered north of these regions (Zhao et al., 2016). The interannual variability of the eddy-covered ice-free area and number in these regions is negatively correlated with the sea level over the continental slope with correlation coefficient equal to −0.7, indicating that it is mainly driven by the intensity of the anticyclonic currents of the BG over the continental slope. The altimetry-based results also show the correlation of eddy statistics with the interannual variability of the freshwater content in the BG. However, the FWC shows a clear rising trend, which is absent in the eddy statistics. As shown by Meneghello et al. (2020), the sea level and the freshwater content do not always correlate, especially in the recent period, which is related to the observed expansion and displacement of the BG (Regan et al., 2019). This indicates that the intensity of the BG is a better predictor of eddy intensity than the freshwater content.

There are several significant limitations associated with the use of altimetry for eddy detection in the Arctic Ocean. First, the amount of altimetry data at a given location varies significantly depending on the presence of sea ice cover and the number and orbit characteristics of working altimeters. For the entire region, the highest number of ice-free measurements is typically from July to October, peaking in August–September. Our estimates of the seasonal eddy frequency peak in September–October are in good agreement with the year-round data of Manley and Hunkins (1985), which also shows a peak in this period. However, in the CS, the observational period extends to November–December due to the inflow of warm Pacific water that keeps the region ice-free for a longer period. The peak in this basin is detected 1 month later—in October–November. Recently, Armitage et al. (2016) have presented a methodology to obtain year-round altimetry sea level data by identifying measurements over temporary open water regions ("leads") between ice flows. These authors were able to obtain dynamic ocean topography in the BS at spatial and temporal resolutions of 1° and 1 month, respectively. Unfortunately, such a resolution is insufficient to investigate mesoscale variability in the Arctic Ocean.

Altimetry can only detect large eddies with strong SLAs, leaving out several other commonly observed eddy types. Since friction with sea ice can dampen eddy velocities near the surface (e.g., Manley & Hunkins, 1985; Meneghello et al., 2021; Ou & Gordon, 1986), the intrahalocline or sub-mixed-layer eddies that can persist under the ice with virtually no surface velocity expressions (Manley & Hunkins, 1985; Zhao et al., 2014)

are not visible to altimeters. Furthermore, the eddies in the marginal ice zone are mostly missing in the altimetry data due to their smaller sizes, contamination of altimetry signals by ice, and the inability to find enclosed contours of sea level even in partly ice-covered areas.

Finally, the eddy identification based on gridded altimetry maps with their relatively coarse spatial resolution is heavily biased toward larger eddies (with a minimum radius of 24 km) with high SLAs. The daily gridded altimetry maps are optimally interpolated and smoothed in time based on rather coarsely spaced data, which can impact the estimations of the eddy trajectories and lifetimes. The comprehensive error estimation of altimetry-derived eddy characteristics in the Arctic Ocean is an important future task. This task, particularly, can be done with the help of the eddy-resolving ocean models, which can be used to simulate sparse altimetry along-track measurements and test their ability to identify eddies compared to full model results. Nonetheless, several cross-validation examples using MODIS Level-3 chl-a and SST data confirm the existence of such eddies and show that their sizes and locations detected in both data sources are similar. These examples suggest that, while there are many resolution issues with altimetry products, they are nonetheless capable of providing valuable information about the eddy field. Thus, these products make a crucial contribution toward more comprehensive monitoring and improved understanding of the eddy field in ice-free regions of the changing Arctic Ocean.

Data Availability Statement

The gridded and along-track satellite altimeter data (product identifiers: SEALEVEL_GLO_PHY_L4_REP_OBSERVATIONS_088_047 and SEALEVEL_GLO_PHY_L3_REP_OBSERVATIONS_008_062) are freely made available by the Copernicus Marine Environmental Monitoring Service (e.g., https://resources.marine.copernicus.eu/?option=com_csw&view=details&product_id=SEALEVEL_GLO_PHY_L4_REP_OBSERVATIONS_008_047). Data on chlorophyll and SST variability are made freely available by NASA Goddard Space Flight Center, Ocean Ecology Laboratory, Ocean Biology Processing Group (Moderate-resolution Imaging Spectroradiometer (MODIS) Aqua Ocean Color Data; 201818 Reprocessing. NASA OB.DAAC, Greenbelt, MD, USA. https://data/10.5067/AQUA/MODIS/L2/OC/2018, https://oceancolor.gsfc.nasa.gov/l3/). MERRA-2 reanalysis data are available from https://disc.gsfc.nasa.gov/datasets?project=MERRA-2. Monthly discharge data of Mackenzie River for 1993–2016 was obtained from the Reference Hydrometric Basin Network, Canada (Brimley et al., 1999) and downloaded from HYDAT database (https://collaboration.cmc.ec.gc.ca/cmc/hydrometrics/www/).

Acknowledgments
Analysis of temporal variability of eddy characteristics was supported by the Russian Foundation for Basic Research (RFBR) grant No. 18-35-20078 mol_a_ved, development of eddy identification method was supported by the Russian Science Foundation (RSF) grant 21-17-00278, investigation of the eddy formation mechanisms was supported by RSF grant 21-77- 00029; analysis of kinematic eddy properties was funded by the U.S. National Science Foundation, grant #1829969. We thank the reviewer Dr. Gianluca Meneghello (MIT) and one anonymous reviewer for their constructive comments. The authors declare no conflict of interests.

References

Armitage, T. W. K., Bacon, S., Ridout, A. L., Petty, A. A., Wolbach, S., & Tsamados, M. (2016). Arctic Ocean surface geostrophic circulation 2003–2014. *The Cryosphere*, *11*(4), 1767–1780. https://doi.org/10.5194/tc-11-1767-2017

Ballarotta, M., Ubelmann, C., Pujol, M.-I., Taburet, G., Fournier, F., Legeais, J.-F., et al. (2019). On the resolutions of ocean altimetry maps. *Ocean Science*, *15*, 1091–1109. https://doi.org/10.5194/os-15-1091-2019

Bashmachnikov, I., Belonenko, T., Kuibin, P., Volkov, D., & Foux, V. (2018). Pattern of vertical velocity in the Lofoten vortex (the Norwegian Sea). *Ocean Dynamics*, *68*(12), 1711–1725. https://doi.org/10.1007/s10236-018-1213-1

Bashmachnikov, I., Kozlov, I. E., Petrenko, L. A., Glock, N. I., & Wekerle, C. (2020). Eddies in the North Greenland Sea and Fram Strait from satellite altimetry, SAR and high-resolution model data. *Journal of Geophysical Research: Oceans*, *125*, e2019JC015832. https://doi.org/10.1029/2019jc015832

Brannigan, L., Johnson, H., Lique, C., Nycander, J., & Nilsson, J. (2017). Generation of subsurface anticyclones at Arctic surface fronts due to a surface stress. *Journal of Physical Oceanography*, *47*(11), 2653–2671. https://doi.org/10.1175/jpo-d-17-0022.1

Brimley, B., Cantin, J. F., Harvey, D., Kowalchuk, M., Marsh, P., Ouarda, T. B. M. J., et al. (1999). *Establishment of the Reference Hydrometric Basin Network (RHBN)*. Ontario: Environment Canada Research Report.

Capet, X., McWilliams, J. C., Molemaker, M. J., & Shchepetkin, A. F. (2008). Mesoscale to submesoscale transition in the California current system. Part I: Flow structure, eddy flux, and observational tests. *Journal of Physical Oceanography*, *38*(1), 29–43. https://doi.org/10.1175/2007jpo3671.1

Carmack, E. C., & Kulikov, E. A. (1998). Wind-forced upwelling and internal Kelvin wave generation in Mackenzie Canyon, Beaufort Sea. *Journal of Geophysical Research*, *103*(C9), 18447–18458. https://doi.org/10.1029/98jc00113

Chaigneau, A., Gizolme, A., & Grados, C. (2008). Mesoscale eddies off Peru in altimeter records: Identification algorithms and eddy spatio-temporal patterns. *Progress in Oceanography*, *79*(2–4), 106–119. https://doi.org/10.1016/j.pocean.2008.10.013

Chaigneau, A., Le Texier, M., Eldin, G., Grados, C., & Pizarro, O. (2011). Vertical structure of mesoscale eddies in the eastern South Pacific Ocean: A composite analysis from altimetry and Argo profiling floats. *Journal of Geophysical Research*, *116*(C11025). https://doi.org/10.1029/2011jc007134

Chelton, D. B., Schlax, M. G., & Samelson, R. M. (2011). Global observations of nonlinear mesoscale eddies. *Progress in Oceanography*, *91*(2), 167–216. https://doi.org/10.1016/j.pocean.2011.01.002

Chen, G., Hou, Y., & Chu, X. (2011). Mesoscale eddies in the South China Sea: Mean properties, spatiotemporal variability, and impact on thermohaline structure. *Journal of Geophysical Research*, *116*, C06018. https://doi.org/10.1029/2010JC006716

Corlett, W. B., & Pickart, R. S. (2017). The Chukchi slope current. *Progress in Oceanography*, *153*, 50–65. https://doi.org/10.1016/j.pocean.2017.04.005

D'Asaro, E. (1988). Observations of small eddies in the Beaufort Sea. *Journal of Geophysical Research*, *93*(6), 6669–6684. https://doi.org/10.1029/JC093iC06p06669

Doddridge, E. W., Meneghello, G., Marshall, J., Scott, J., & Lique, C. (2019). A three-way balance in the Beaufort Gyre: the ice-ocean governor, wind stress, and eddy diffusivity. *Journal of Geophysical Research: Oceans*, *124*, 3107–3124. https://doi.org/10.1029/2018jc014897

Elkin, D. N., & Zatsepin, A. G. (2014). Laboratory study of a shear instability of an alongshore sea current. *Oceanology*, *54*(5), 576–582. https://doi.org/10.1134/s000143701405004x

Faghmous, J., Frenger, I., Yao, Y., Warmka, R., Lindell, A., & Kumar, V. (2015). A daily global mesoscale ocean eddy dataset from satellite altimetry. *Scientific Data*, *2*, 150028. https://doi.org/10.1038/sdata.2015.28

Fine, E. C., MacKinnon, J. A., Alford, M. H., & Mickett, J. B. (2018). Microstructure observations of turbulent heat fluxes in a warm-core Canada Basin eddy. *Journal of Physical Oceanography*, *48*, 2397–2418. https://doi.org/10.1175/jpo-d-18-0028.1

Gelaro, R., McCarty, W., Suárez, M. J., Todling, R., Molod, A., Takacs, L., et al. (2017). The Modern-Era Retrospective Analysis for Research and Applications, Version 2 (MERRA-2). *Journal of Climate*, *30*(14), 5419–5454.

Kirillov, S., Dmitrenko, I., Tremblay, B., Gratton, Y., Barber, D., & Rysgaard, S. (2016). Upwelling of Atlantic water along the Canadian Beaufort Sea continental slope: Favorable atmospheric conditions and seasonal and interannual variations. *Journal of Climate*, *29*(12), 4509–4523. https://doi.org/10.1175/jcli-d-15-0804.1

Kozlov, I. E., Artamonova, A. V., Manucharyan, G. E., & Kubryakov, A. A. (2019). Eddies in the Western Arctic Ocean from spaceborne SAR observations over open ocean and marginal ice zones. *Journal of Geophysical Research: Oceans*, *124*(9), 6601–6616. https://doi.org/10.1029/2019jc015113

Kozlov, I. E., Plotnikov, E. V., & Manucharyan, G. E. (2020). Brief Communication: Mesoscale and submesoscale dynamics in the marginal ice zone from sequential synthetic aperture radar observations. *The Cryosphere*, *14*(9), 2941–2947. https://doi.org/10.5194/tc-14-2941-2020

Kubryakov, A. A., & Stanichny, S. V. (2015a). Mesoscale Eddies in the Black Sea from altimetry data. *Океанология*, *55*(1), 65–77. https://doi.org/10.7868/s0030157415010104

Kubryakov, A. A., & Stanichny, S. V. (2015b). Seasonal and interannual variability of the Black Sea eddies and its dependence on characteristics of the large-scale circulation. *Deep Sea Research I: Oceanographic Research Papers*, *97*, 80–91. https://doi.org/10.1016/j.dsr.2014.12.002

Kubryakov, A. A., Stanichny, S. V., Zatsepin, A. G., & Kremenetskiy, V. V. (2016). Long-term variations of the Black Sea dynamics and their impact on the marine ecosystem. *Journal of Marine Systems*, *163*, 80–94. https://doi.org/10.1016/j.jmarsys.2016.06.006

Larichev, V. D., & Held, I. M. (1995). Eddy amplitudes and fluxes in a homogeneous model of fully developed baroclinic instability. *Journal of Physical Oceanography*, *25*(10), 2285–2297. https://doi.org/10.1175/1520-0485(1995)025<2285:eaafia>2.0.co;2

Le Traon, P. Y., Nadal, F., & Ducet, N. (1998). An improved mapping method of multisatellite altimeter data. *Journal of Atmospheric and Oceanic Technology*, *15*(2), 522–534. https://doi.org/10.1175/1520-0426(1998)015<0522:aimmom>2.0.co;2

Manley, T. O., & Hunkins, K. (1985). Mesoscale eddies of the Arctic Ocean. *Journal of Geophysical Research*, *90*(C3), 4911. https://doi.org/10.1029/jc090ic03p04911

Manucharyan, G. E., & Spall, M. A. (2015). Wind-driven freshwater buildup and release in the Beaufort Gyre constrained by mesoscale eddies. *Geophysical Research Letters*, *42*, 273–282. https://doi.org/10.1002/2015GL065957

Manucharyan, G. E., Thompson, A. F., & Spall, M. A. (2017). Eddy memory mode of multidecadal variability in residual-mean ocean circulations with application to the Beaufort Gyre. *Journal of Physical Oceanography*, *47*(4), 855–866. https://doi.org/10.1175/jpo-d-16-0194.1

Manucharyan, G. E., & Timmermans, M.-L. (2014). Generation and separation of mesoscale eddies from surface ocean fronts. *Journal of Physical Oceanography*, *43*(12), 2545–2562. https://doi.org/10.1175/JPO-D-13-094.1

Mathis, J. T., Pickart, R. S., Hansell, D. A., Kadko, D., & Bates, N. R. (2007). Eddy transport of organic carbon and nutrients from the Chukchi shelf: Impact on the upper halocline of the western Arctic Ocean. *Journal of Geophysical Research*, *112*(C05011). https://doi.org/10.1029/2006jc003899

McGillicuddy, D. J., Jr, & Robinson, A. R. (1997). Eddy-induced nutrient supply and new production in the Sargasso Sea. *Deep Sea Research Part I: Oceanographic Research Papers*, *44*(8), 1427–1450. https://doi.org/10.1016/s0967-0637(97)00024-1

McWilliams, J. C. (2016). Submesoscale currents in the ocean. *Proceedings of the Royal Society A*, *472*(2189), 20160117. https://doi.org/10.1098/rspa.2016.0117

Meneghello, G., Doddridge, E., Marshall, J., Scott, J., & Campin, J.-M. (2020). Exploring the role of the "ice-ocean governor" and mesoscale eddies in the equilibration of the Beaufort Gyre: lessons from observations. *Journal of Physical Oceanography*, *50*(1), 269–277. https://doi.org/10.1175/jpo-d-18-0223.1

Meneghello, G., Marshall, J., Campin, J. M., Doddridge, E., & Timmermans, M. L. (2018). The ice-ocean governor: Ice-ocean stress feedback limits Beaufort Gyre spin-up. *Geophysical Research Letters*, *45*, 293–299. https://doi.org/10.1029/2018GL080171

Meneghello, G., Marshall, J., Cole, S. T., & Timmermans, M. L. (2017). Observational inferences of lateral eddy diffusivity in the halocline of the Beaufort Gyre. *Geophysical Research Letters*, *44*(24), 331–338. https://doi.org/10.1002/2017gl075126

Meneghello, G., Marshall, J., Lique, C., Isachsen, P. E., Doddridge, E., Campin, J.-M., et al. (2021). Genesis and Decay of Mesoscale Baroclinic eddies in the seasonally ice-covered interior Arctic Ocean. *Journal of Physical Oceanography*, *51*(1), 115–129. https://doi.org/10.1175/jpo-d-20-0054.1

Mensa, J. A., Timmermans, M.-L., Kozlov, I. E., Williams, W. J., & Özgökmen, T. (2018). Surface drifter observations from the Arctic Ocean's Beaufort Sea: Evidence for submesoscale dynamics. *Journal of Geophysical Research: Oceans*, *122*(12), 9455–9475. https://doi.org/10.1002/2017JC013728

Muench, R. D., Gunn, J. T., Whitledge, T. E., Schlosser, P., & Smethie, W. (2000). An Arctic Ocean cold core eddy. *Journal of Geophysical Research*, *105*(C10), 23997–24006. https://doi.org/10.1029/2000jc000212

Mulligan, R. P., & Perrie, W. (2019). Circulation and structure of the Mackenzie River plume in the coastal Arctic Ocean. *Continental Shelf Research*, *177*, 59–68. https://doi.org/10.1016/j.csr.2019.03.006

Naumov, L., Gordeeva, S., & Belonenko, T. (2019). Quality assessment of a satellite altimetry data product DT18 in the Norwegian Sea: A comparison to tide gauge records and drifters data. *Advances in Space Research*. https://doi.org/10.1016/j.asr.2019.09.029

Newton, J. L., Aagaard, K., & Coachman, L. K. (1974). Baroclinic eddies in the Arctic Ocean. *Deep Sea Research and Oceanographic Abstracts*, *21*(9), 707–719. https://doi.org/10.1016/0011-7471(74)90078-3

Nghiem, S. V., Hall, D. K., Rigor, I. G., Li, P., & Neumann, G. (2014). Effects of Mackenzie River discharge and bathymetry on sea ice in the Beaufort Sea. *Geophysical Research Letters*, *41*(3), 873–879. https://doi.org/10.1002/2013gl058956

Nurser, A. J. G., & Bacon, S. (2014). The Rossby radius in the Arctic Ocean. *Ocean Science*, *10*(6), 967–975. https://doi.org/10.5194/os-10-967-2014

Ou, H. W., & Gordon, A. L. (1986). Spin-down of baroclinic eddies under sea ice. *Journal of Geophysical Research*, *91*(C6), 7623–7630. https://doi.org/10.1029/JC091iC06p07623

Ovchinnikov, I. M., & Plakhin, E. (1976). *Hydrology of the Mediterranean Sea*. Leningrad: Gidrometeoizdat.

Padman, L., Levine, M., Dillon, T., Morison, J., & Pinkel, R. (1990). Hydrography and microstructure of an Arctic cyclonic eddy. *Journal of Geophysical Research*, *95*(C6), 9411–9719. https://doi.org/10.1029/jc095ic06p09411

Pascual, A., Faugère, Y., Larnicol, G., & Le Traon, P.-Y. (2006). Improved description of the ocean mesoscale variability by combining four satellite altimeters. *Geophysical Research Letters*, *33*(2). https://doi.org/10.1029/2005gl024633

Pickart, R. S., Spall, M. A., & Mathis, J. T. (2013). Dynamics of upwelling in the Alaskan Beaufort Sea and associated shelf-basin fluxes. *Deep Sea Research Part I: Oceanographic Research Papers*, *76*, 35–51. https://doi.org/10.1016/j.dsr.2013.01.007

Pickart, R. S., Weingartner, T. J., Pratt, L. J., Zimmermann, S., & Torres, D. J. (2005). Flow of winter-transformed Pacific water into the Western Arctic. *Deep Sea Research Part II: Topical Studies in Oceanography*, *52*(24–26), 3175–3198. https://doi.org/10.1016/j.dsr2.2005.10.009

Proshutinsky, A., Krishfield, R., Toole, J. M., Timmermans, M.-L., Williams, W., Zimmermann, S., et al. (2019). Analysis of the Beaufort Gyre freshwater content in 2003–2018. *Journal of Geophysical Research: Oceans*, *124*, 9658– 9689. https://doi.org/10.1029/2019JC015281

Raj, R. P., Johannessen, J. A., Eldevik, T., Nilsen, J. E. Ø., & Halo, I. (2016). Quantifying mesoscale eddies in the Lofoten Basin. *Journal of Geophysical Research: Oceans*, *121*(7), 4503–4521. https://doi.org/10.1002/2016jc011637

Regan, H. C., Lique, C., & Armitage, T. W. K. (2019). The Beaufort Gyre extent, shape, and location between 2003 and 2014 from satellite observations. *Journal of Geophysical Research: Oceans*, *124*(2), 844–862. https://doi.org/10.1029/2018jc014379

Sadarjoen, I., & Post, F. H. (2000). Detection, quantification, and tracking of vortices using streamline geometry. *Computers and Graphics*, *24*(3), 333–341. https://doi.org/10.1016/s0097-8493(00)00029-7

Scott, R. M., Pickart, R. S., Lin, P., Münchow, A., Li, M., Stockwell, D. A., & Brearley, J. A. (2019). Three-Dimensional Structure of a Cold-Core Arctic Eddy Interacting with the Chukchi Slope Current. *Journal of Geophysical Research: Oceans*, *124*(11), 8375–8391. https://doi.org/10.1029/2019jc015523

Sévigny, C., Gratton, Y., & Galbraith, P. S. (2015). Frontal structures associated with coastal upwelling and ice-edge subduction events in southern Beaufort Sea during the Canadian Arctic Shelf Exchange Study. *Journal of Geophysical Research: Oceans*, *120*(4), 2523–2539. https://doi.org/10.1002/2014jc010641

Smith, K. S., & Vallis, G. K. (2001). The scales and equilibration of midocean eddies: Freely evolving flow. *Journal of Physical Oceanography*, *31*(2), 554–571. https://doi.org/10.1175/1520-048510.1175/1520-0485(2001)031<0554:tsaeom>2.0.co;2

Souza, J. M. A. C., de Boyer Montégut, C., & Le Traon, P. Y. (2011). Comparison between three implementations of automatic identification algorithms for the quantification and characterization of mesoscale eddies in the South Atlantic Ocean. *Ocean Science*, *7*(3), 317–334. https://doi.org/10.5194/os-7-317-2011

Spall, M. A. (1995). Frontogenesis, subduction, and cross-front exchange at upper ocean fronts. *Journal of Geophysical Research*, *100*(C2), 2543. https://doi.org/10.1029/94jc02860

Spall, M. A. (2008). Circulation and water mass transformation in a model of the Chukchi Sea. *Journal of Geophysical Research*, *112*(C5). https://doi.org/10.1029/2005jc003364

Spall, M. A., Pickart, R. S., Fratantoni, P. S., & Plueddemann, A. J. (2008). Western Arctic shelf break eddies: Formation and transport. *Journal of Physical Oceanography*, *38*(8), 1644–1668. https://doi.org/10.1175/2007jpo3829.1

Spall, M. A., Pickart, R. S., Li, M., Itoh, M., Lin, P., Kikuchi, T., & Qi, Y. (2018). Transport of Pacific water into the Canada Basin and the formation of the Chukchi Slope Current. *Journal of Geophysical Research: Oceans*, *123*(10), 7453–7471. https://doi.org/10.1029/2018jc013825

Timmermans, M. -L., & Marshall, J. (2020). Understanding Arctic Ocean circulation: A review of ocean dynamics in a changing climate. *Journal of Geophysical Research: Oceans*, *125*, e2018JC014378. https://doi.org/10.1029/2018jc014378

Timmermans, M.-L., Melling, H., & Rainville, L. (2007). Dynamics in the deep Canada Basin, Arctic Ocean, inferred by thermistor chain time series. *Journal of Physical Oceanography*, *37*(4), 1066–1076. https://doi.org/10.1175/jpo3032.1

Timmermans, M.-L., Toole, J., Proshutinsky, A., Krishfield, R., & Plueddemann, A. (2008). Eddies in the Canada Basin, Arctic Ocean, observed from ice-tethered profilers. *Journal of Geophysical Research: Oceans*, *38*(1), 133–145. https://doi.org/10.1175/2007jpo3782.1

Volkov, D. L., Landerer, F. W., & Kirillov, S. A. (2013). The genesis of sea level variability in the Barents Sea. *Continental Shelf Research*, *66*, 92–104. https://doi.org/10.1016/j.csr.2013.07.007

Volkov, D. L., & Pujol, M. (2012). Quality assessment of a satellite altimetry data product in the Nordic, Barents, and Kara seas. *Journal of Geophysical Research*, *117*(C3). https://doi.org/10.1029/2011jc007557

Watanabe, E. (2011). Beaufort shelf break eddies and shelf-basin exchange of Pacific summer water in the western Arctic Ocean detected by satellite and modeling analyses. *Journal of Geophysical Research*, *116*, C08034. https://doi.org/10.1029/2010JC006259

Watanabe, E., Kishi, M. J., Ishida, A., & Aita, M. N. (2012). Western Arctic primary productivity regulated by shelf-break warm eddies. *Journal of Oceanography*, *68*(5), 703–718. https://doi.org/10.1007/s10872-012-0128-6

Watanabe, E., Onodera, J., Harada, N., Honda, M. C., Kimoto, K., Kikuchi, T., et al. (2014). Enhanced role of eddies in the Arctic marine biological pump. *Nature Communications*, *5*, 3950. https://doi.org/10.1038/ncomms4950

Weingartner, T. J., Danielson, S., Sasaki, Y., Pavlov, V., & Kulakov, M. (1999). The Siberian Coastal Current: a wind and buoyancy-forced Arctic coastal current. *Journal of Geophysical Research*, *104*(C12), 697–713. https://doi.org/10.1029/1999jc900161

Whitehead, J. A., & Miller, A. R. (1979). Laboratory simulation of the gyre in the Alboran Sea. *Journal of Geophysical Research*, *84*(C7), 3733. https://doi.org/10.1029/jc084ic07p03733

Wood, K. R., Bond, N. A., Danielson, S. L., Overland, J. E., Salo, S. A., Stabeno, P. J., & Whitefield, J. (2015). A decade of environmental change in the Pacific Arctic region. *Progress in Oceanography*, *136*, 12–31. https://doi.org/10.1016/j.pocean.2015.05.005

Yang, D., Shi, X., & Marsh, P. (2015). Variability and extreme of Mackenzie River daily discharge during 1973-2011. *Quaternary International*, *380–381*, 159–168. https://doi.org/10.1016/j.quaint.2014.09.023

Zatsepin, A., Kubryakov, A., Aleskerova, A., Elkin, D., & Kukleva, O. (2019). Physical mechanisms of submesoscale eddies generation: Evidences from laboratory modeling and satellite data in the Black Sea. *Ocean Dynamics*, *69*(2), 253–266. https://doi.org/10.1007/s10236-018-1239-4

Zhao, M., Timmermans, M.-L., Cole, S., Krishfield, R., Proshutinsky, A., & Toole, J. (2014). Characterizing the eddy field in the Arctic Ocean halocline. *Journal of Geophysical Research: Oceans*, *119*(12), 8800–8817. https://doi.org/10.1002/2014jc010488

Zhao, M., Timmermans, M.-L., Cole, S., Krishfield, R., & Toole, J. (2016). Evolution of the eddy field in the Arctic Ocean's Canada Basin, 2005-2015. *Geophysical Research Letters*, *43*(15), 8106–8114. https://doi.org/10.1002/2016gl069671